Reduced order variational multiscale enrichment method for thermo-mechanical problems

Shuhai Zhang* and Caglar Oskay†

Department of Civil and Environmental Engineering
Vanderbilt University
Nashville, TN 37235

Abstract

This manuscript presents the formulation and implementation of the reduced order variational multiscale enrichment (ROVME) method for thermo-mechanical problems. ROVME is extended to model the inelastic behavior of heterogeneous structures, in which the constituent properties are temperature sensitive. The temperature-dependent coefficient tensors of the reduced order method are approximated in an efficient manner, retaining the computational efficiency of the reduced order model in the presence of spatial/temporal temperature variations. A Newton-Raphson iterative scheme is formulated and implemented for the numerical evaluation of nonlinear system of equations associated with the proposed ROVME method. Numerical verifications are performed to assess the efficiency and accuracy of the proposed computational framework. The results of the verifications reveal that ROVME retains reasonable accuracy and achieves high efficiency in the presence of thermo-mechanical loads.

Keywords: Multiscale modeling, Thermo-mechanical modeling, Variational multiscale enrichment; Reduced order modeling, Elasto-viscoplastic.

1 Introduction

Performance of structures operating in extreme thermo-mechanical environments is typically marked by the formation of hot-spots. Hot-spots refer to localized regions within the domain of the structure that are exposed to higher rates of heating, higher stresses or a combination

---

*Department of Civil and Environmental Engineering, Vanderbilt University, Nashville, TN 37235, United States. Email: shuhai.zhang@vanderbilt.edu

†Corresponding author address: VU Station B#351831, 2301 Vanderbilt Place, Nashville, TN 37235. Email: caglar.oskay@vanderbilt.edu

of both. Hot-spots are considered important as they serve as failure initiation sites (such as, shock-boundary layer interaction-induced localized heating in hypersonic aircraft components [51, 43, 38]), and could ultimately define structural survivability.

From the modeling perspective, deformation and failure mechanisms within hot-spots may be accurately captured using thermo-mechanical multiscale computational approaches, where the microstructural heterogeneities are resolved at least within a critical subdomain of the structure. The majority of the previous efforts on thermo-mechanical multiscale modeling employed computational homogenization principles (e.g., Golanski et al. [18], Ghosh et al. [17, 31], Yu and Fish [53], Zhang et al. [55], Ozdemir et al. [44], Muliana et al. [35, 36]), which are valid at the scale separation limit. On the other hand, global-local methods, including the global-local finite element method [33, 37, 28, 14, 16], the domain decomposition method [26], the generalized finite element method [10], Lagrange multiplier based multiscale method [29], numerical subgrid algorithms [4, 5], among others, are more appropriate for problems that exhibit poor or no scale separation. These approaches admit higher resolution within the hotspots, while coarse discretization is employed within the rest of the structural domain. The variational multiscale enrichment (VME) method [40, 41, 56] is a global-local method that addresses problems in which the detailed resolution of the material microstructure is considered within localized regions of interest. Rooted in the variational multiscale method [19, 20], VME is a multiscale numerical subgrid algorithm that relies on the additive decomposition of the cardinal response fields (e.g., displacement) into coarse and fine scale counterparts within the variational setting.

Evolution of large-sized problems in which the microstructural heterogeneities are resolved either based on homogenization or global-local methods are well-known to be computationally very expensive, and often times prohibitive. This issue is typically overcome using massively parallel simulations (e.g., [32]), reduced order approximations to the microstructure problems, or a combination of both. In the context of homogenization methods, a number of order reduction approaches, such as generalized method of cells [2], transformation field analysis [11, 30, 15], fast Fourier transforms (FFT) [34], proper orthogonal decomposition [54, 39] and eigendeformation-based model order reduction [42, 58], among others were successful in reducing the complexity of microstructure computation for linear and nonlinear problems. In the context of global-local methods, FFT was employed to model the thermo-elastic behavior of alumina/Al composites [25, 3]. The reduced order variational multiscale enrichment (ROVME) [57] was recently proposed by the authors to improve the computational efficiency of the VME method [56]. Derived from the eigendeformation-based reduced order approach, ROVME was shown to efficiently reduce computational complexity by two orders of magnitude when applied to deformation problems involving material nonlinearity. Application of the principles of ROVME to address thermo-mechanical problems presents additional challenges. The primary

difficulty is that the construction of the reduced order basis (via microstructural influence functions) depends on the elastic properties of the constituents. Spatio-temporal variation of temperature within a thermo-mechanically loaded structure therefore requires continuous basis reconstruction when the elastic properties are temperature-dependent. The computational expense of the recurrent basis reconstructions may offset the computational efficiency gains to a significant degree.

The current manuscript extends the reduced order variational multiscale enrichment method to address thermo-mechanical problems that exhibit global-local character. The thermo-mechanical coupling effect due to the presence of thermal expansions, temperature-dependent mechanical inelastic properties, as well as the elastic properties is taken into account [1, 27, 22]. A key novel contribution of the present manuscript is the efficient approximation of the temperature dependence of the reduced order model coefficients, which allows the thermo-mechanical ROVME to retain the computational efficiency. Numerical studies are performed to verify the proposed method against direct numerical simulations, and demonstrate its capability in capturing the thermo-mechanical behavior of heterogeneous structures.

The remainder of the manuscript is organized as follows: Section 2 provides the problem statement and governing equations of the elasto-viscoplastic problem. Sections 3 and 4 describe the formulation of the VME and ROVME methods for thermo-mechanical problems, respectively. Section 5 details the implementation strategy. Sections 6 and 7 present numerical simulations which demonstrate the accuracy and capability of the proposed methodology. The conclusions are discussed in Section 8.

2   Problem Statement

The domain of the structure is denoted by $\Omega \subset \mathbb{R}^{n_{\text{sd}}}$ (n_{sd} is the number of spatial dimensions) as shown in Fig. 1, the equilibrium equation within the problem domain is expressed as:

$$\nabla \cdot \boldsymbol{\sigma}(\mathbf{x}, T, t) = 0; \quad \mathbf{x} \in \Omega, \ t \in [0, \ t_e] \tag{1}$$

where, $\mathbf{x}$ and t are the position and time coordinates, respectively; T the temperature; $\boldsymbol{\sigma}$ the stress tensor; $\nabla \cdot (\cdot)$ the divergence operator and t_e the end of the observation period. The body force is taken to be negligible compared with the external force. The constitutive behavior is expressed as:

$$\boldsymbol{\sigma}(\mathbf{x}, T, t) = \mathbf{L}(\mathbf{x}, T) : \left[\boldsymbol{\varepsilon}(\mathbf{x}, T, t) - \boldsymbol{\varepsilon}^{vp}(\mathbf{x}, T, t) - \boldsymbol{\varepsilon}^T(\mathbf{x}, T) \right] \tag{2}$$

in which, $\mathbf{L}$ is the temperature-dependent tensor of elastic moduli; $\boldsymbol{\varepsilon}^{vp}$ and $\boldsymbol{\varepsilon}^T$ denote the viscoplastic and thermal strains, respectively; and (:) is the double inner product. The thermal
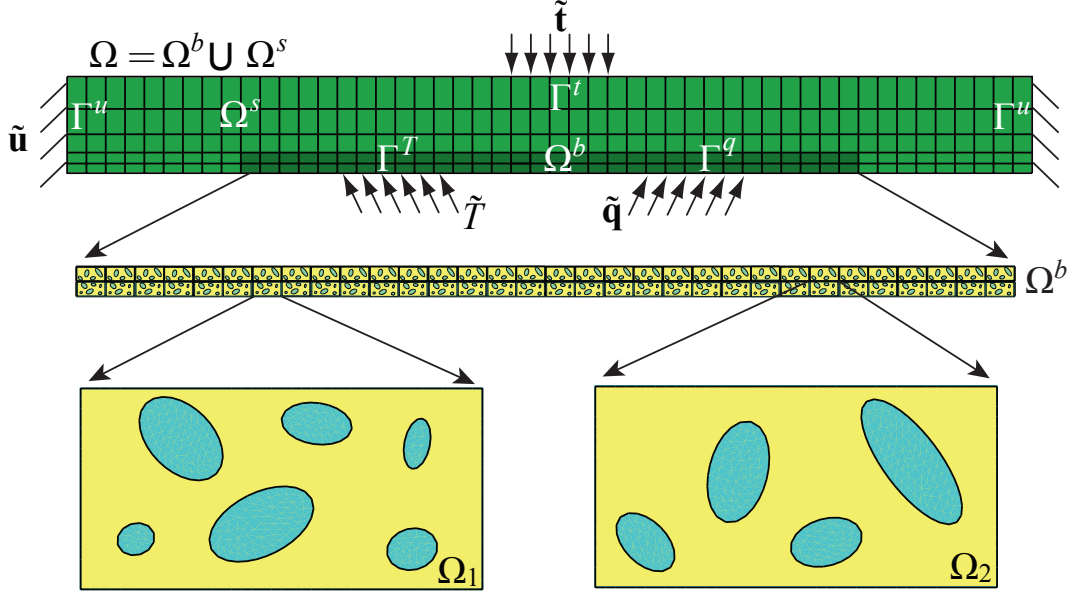
Figure 1: The schematic representation of the overall problem domain (Ω), enrichment region (Ω_b) and two representative enrichment domains (Ω_1 and Ω_2).

strain is expressed as:

$$\boldsymbol{\varepsilon}^T(\mathbf{x}, T) = \boldsymbol{\alpha}^T(\mathbf{x})\left[T(\mathbf{x}) - T_0\right] \tag{3}$$

where, T_0 is the reference temperature; and $\boldsymbol{\alpha}^T$ the tensor of thermal expansion coefficients. The evolution of the inelastic strain is expressed in the functional form:

$$\dot{\boldsymbol{\varepsilon}}^{vp} = \Phi\left(\boldsymbol{\sigma}, \boldsymbol{\varepsilon}^{vp}, T, \mathbf{q}; \mathbf{k}\right) \tag{4}$$

in which, $\mathbf{q}$ denotes the vector of internal state variables that represent the internal deformation mechanisms characterizing the inelastic processes, and $\mathbf{k}$ is the set of material properties associated with the inelastic flow. The specific forms of the evaluation laws of the internal state variables are provided in Section 6 in the context of numerical examples. As further explained below, we are interested in the detailed response within a characteristic subdomain ($\Omega_b \subset \Omega$), where the material microstructure with multiple constituents is resolved. The overall constitutive model form (i.e., Eqs. (2)-(4)) is taken to be the same for all constituents, whereas the model parameters and evolution equations (i.e., $\mathbf{L}, \boldsymbol{\alpha}, \mathbf{k}, \mathbf{q}$ and Φ) could be different for each constituent. The boundary conditions of the mechanical problem are:

$$\mathbf{u}(\mathbf{x}, t) = \tilde{\mathbf{u}}(\mathbf{x}, t); \qquad \mathbf{x} \in \Gamma^u \tag{5}$$

$$\boldsymbol{\sigma}(\mathbf{x}, t) \cdot \mathbf{n} = \tilde{\mathbf{t}}(\mathbf{x}, t); \qquad \mathbf{x} \in \Gamma^t \tag{6}$$

4

where, $\tilde{\mathbf{u}}$ is the prescribed displacement along the Dirichlet boundary, Γ^u, and $\tilde{\mathbf{t}}$ is the pre-scribed traction along the Neumann boundary, Γ^t. The external boundary decomposition is performed such that $\partial\Omega = \Gamma = \Gamma^u \cup \Gamma^t$ and $\Gamma^u \cap \Gamma^t \equiv \emptyset$.

The thermal state of the structure is defined by the steady state conditions:

$$\nabla \cdot [\mathbf{K}(\mathbf{x}) \cdot \nabla T(\mathbf{x}, t)] = 0; \qquad \mathbf{x} \in \Omega \tag{7}$$

subjected to

$$T(\mathbf{x}, t) = \tilde{T}(\mathbf{x}, t); \qquad \mathbf{x} \in \Gamma^T \tag{8}$$

$$\mathbf{K} \cdot \nabla T = \tilde{\mathbf{q}}(\mathbf{x}, t); \qquad \mathbf{x} \in \Gamma^q \tag{9}$$

where, $\mathbf{K}$ is thermal conductivity tensor; $\tilde{T}$ and $\tilde{\mathbf{q}}$ denote boundary temperature and flux data along the respective boundaries. The time variation of temperature is due to time-dependent boundary conditions, which is taken to be independent of the mechanical response. The transients are taken to occur at time scales significantly shorter than the time scales at which mechanical loads are applied, and therefore neglected in this study.

3 Variational Multiscale Enrichment (VME)

The VME formulation of the mechanical response of inelastically deforming solids, and coupled mechanical-diffusion of elastically deforming solids are discussed in detail in Refs. [56] and [43], respectively. In what follows, the VME equations for the temperature-dependent mechanical problem are summarized, since the VME formulation forms the basis of the ROVME implementation.

The domain of the structure $\Omega \subset \mathbb{R}^{n_{\mathrm{sd}}}$ is decomposed into two non-overlapping subdomains, of which the enrichment region is further discretized into a series of non-overlapping enrichment (microstructural) domains:

$$\Omega = \Omega_s \cup \Omega_b; \quad \Omega_s \cap \Omega_b \equiv \emptyset \tag{10a}$$

$$\Omega_b = \bigcup_{\alpha=1}^{n_{\mathrm{en}}} \Omega_\alpha; \quad \Omega_\alpha \cap \Omega_\beta \equiv \emptyset \text{ when } \alpha \neq \beta \tag{10b}$$

where, Ω_s and Ω_b denote the substrate region and the enrichment region, respectively. n_{en} denotes the total number of enrichment domains in the structure. The microstructural hetero-geneity is resolved only in the enrichment region, while using a "homogenized" microstructure in the substrate region. The geometry of each of the enrichment domains is taken such that it can be represented by a classical macroscale finite element.

The mechanical displacement field is decomposed into macroscale and microscale compo-

nents through additive two-scale decomposition:

$$\mathbf{u}(\mathbf{x}, T, t) = \mathbf{u}^M(\mathbf{x}, T, t) + \sum_{\alpha=1}^{n_{en}} \mathcal{H}(\Omega_\alpha) \mathbf{u}_\alpha^m(\mathbf{x}, T, t) \tag{11}$$

where, $\mathbf{u}^M \in \mathcal{V}^M(\Omega)$ and $\mathbf{u}_\alpha^m \in \mathcal{V}_\alpha(\Omega_\alpha)$ are respectively the macroscale and microscale displacement fields associated with the enrichment domain, Ω_α, which are evaluated within the variational setting. The Heaviside function, $\mathcal{H}(\Omega_\alpha)$ ($\mathcal{H}=1$ if $\mathbf{x} \in \Omega_\alpha$, while $\mathcal{H}=0$ elsewhere), is employed to ensure the microscale displacement field ($\mathbf{u}_\alpha^m$) only contributes to the displacement field on the closure of the associated enrichment domain, Ω_α. $\mathcal{V}^M$ and $\mathcal{V}_\alpha$ denote the trial spaces for the macro- and microscale fields, respectively (specialization from infinite to finite dimensional approximation is skipped for brevity):

$$\mathcal{V}^M(\Omega) \equiv \left\{ \mathbf{u}^M(\mathbf{x}, T, t) \middle| \ \mathbf{u}^M = \sum_{A=1}^{N_D} N_A(\mathbf{x}) \ \hat{\mathbf{u}}_A^M(T, t); \ \hat{\mathbf{u}}_A^M = \tilde{\mathbf{u}}(\mathbf{x}_A, t) \text{ if } \mathbf{x}_A \in \Gamma^u \right\} \tag{12}$$

$$\mathcal{V}_\alpha(\Omega_\alpha) \equiv \left\{ \mathbf{u}_\alpha^m(\mathbf{x}, T, t) \middle| \ \mathbf{u}_\alpha^m = \sum_{a=1}^{n_{d_\alpha}} n_{\alpha,a}(\mathbf{x}) \ \hat{\mathbf{u}}_{\alpha,a}^m(T, t); \ \hat{\mathbf{u}}_{\alpha,a}^m = 0 \text{ if } \mathbf{x}_\alpha \in \Gamma_\alpha^u \right\} \tag{13}$$

in which, N_D and n_{d_α} are the number of nodes associated with the finite element bases in the macroscale discretization of Ω, and the microscale discretization of Ω_α, respectively; N_A and $n_{\alpha,a}$ are the shape functions for the macroscale and microscale fields, respectively; $\mathbf{x}_A$ and $\mathbf{x}_a$ are the corresponding nodal coordinates. Overhat denotes the nodal coefficients of the corresponding response field.

The macro- and microscale shape functions are chosen such that the solution space is the direct sum of the macro- and microscale solution spaces [20, 56], to ensure solution uniqueness and stability in view of the displacement decomposition of Eq. (11) [16, 21]. In the current manuscript, homogeneous Dirichlet boundary conditions are employed along the enrichment domain boundaries (Eq. (13)) [7]. Other microscale boundary conditions have also been proposed previously to achieve higher accuracy [41, 56]. Similar to the displacement field decomposition in Eq. (11), the test function is additively decomposed into macroscale ($\mathbf{w}^M$) and microscale ($\mathbf{w}_\alpha^m$) components [56, 57].

Considering the additive decomposition of the displacement field and test function, the governing equation in the weak form is decomposed into macroscale and microscale problems. The macroscale equilibrium in the weak form is obtained from Eq. (1) by considering vanishing microscale test functions:

$$\int_\Omega \nabla \mathbf{w}^M : \boldsymbol{\sigma} \left(\mathbf{u}^M, \{\mathbf{u}_i^m\}_1^{n_{en}} \right) \ d\Omega - \int_{\Gamma^t} \mathbf{w}^M \cdot \tilde{\mathbf{t}} \ d\Gamma = 0 \tag{14}$$

Setting the macroscale test functions to zero, the weak form of the microscale problem at an arbitrary enrichment domain, Ω_α, is obtained:

$$\int_{\Omega_\alpha} \nabla \mathbf{w}_\alpha^m : \boldsymbol{\sigma}(\mathbf{u}^M, \mathbf{u}_\alpha^m) \, d\Omega = 0; \quad \alpha = 1, 2, ...n_{\text{en}}. \tag{15}$$

The macroscale and microscale problems are coupled through the stress field, which is a function of both macro- and micro- displacement components. Due to the inelastic, nonlinear and history-dependent constitutive behavior, the stress field does not admit convenient scale decomposition.

Similar to the mechanical problem, the temperature field is decomposed into macro- and microscale components:

$$T(\mathbf{x}, t) = T^M(\mathbf{x}, t) + \sum_{\alpha=1}^{n_{\text{en}}} \mathcal{H}(\Omega_\alpha) \, T_\alpha^m(\mathbf{x}, t) \tag{16}$$

where, $T^M \in \mathcal{W}^M(\Omega)$ and $T_\alpha^m \in \mathcal{W}_\alpha(\Omega_\alpha)$ are the macroscale and microscale temperature fields, respectively. $\mathcal{W}^M$ and $\mathcal{W}_\alpha$ are the trial spaces for the macro- and microscale temperatures:

$$\mathcal{W}^M(\Omega) \equiv \left\{ T^M(\mathbf{x}, t) \middle| \; T^M = \sum_{A=1}^{N_D} N_A(\mathbf{x}) \, \hat{T}_A^M(T, t); \; \hat{T}_A^M = \tilde{T}(\mathbf{x}_A, t) \text{ if } \mathbf{x}_A \in \Gamma^T \right\} \tag{17}$$

$$\mathcal{W}_\alpha(\Omega_\alpha) \equiv \left\{ T_\alpha^m(\mathbf{x}, t) \middle| \; T_\alpha^m = \sum_{a=1}^{n_{d_\alpha}} n_{\alpha,a}(\mathbf{x}) \, \hat{T}_{\alpha,a}^m(T, t); \; \hat{T}_{\alpha,a}^m = 0 \text{ if } \mathbf{x}_\alpha \in \Gamma_\alpha^q \right\} \tag{18}$$

Correspondingly, the steady state thermal problem (Eqs. (7)-(9)) yields a macroscale problem,

$$\int_\Omega \nabla v^M \cdot \mathbf{K} \cdot \nabla T^M \, d\Omega = \int_{\Gamma^q} v^M \cdot \tilde{\mathbf{q}} \, d\Gamma - \sum_{\alpha=1}^{n_{\text{en}}} \int_{\Omega_\alpha} \nabla v^M \cdot \mathbf{K} \cdot \nabla T_\alpha^m \, d\Omega \tag{19}$$

and a series of microscale problems,

$$\int_{\Omega_\alpha} \nabla v_\alpha^m \cdot \mathbf{K} \cdot \nabla T_\alpha^m \, d\Omega = -\int_{\Omega_\alpha} \nabla v_\alpha^m \cdot \mathbf{K} \cdot \nabla T^M \, d\Omega; \quad \alpha = 1, 2, ...n_{\text{en}}. \tag{20}$$

where, v^M and v_α^m are the macro- and microscale temperature test functions, respectively.

For both thermal and mechanical problems, the macroscale system and microscale problems are solved iteratively until convergence is achieved at a given time step. In the enrichment region, stress and strain fields are updated at each integration point of the microscale discretization. Therefore, the computational complexity of VME is proportional to the number of enrichment domains within the enrichment region as well as the complexity of the microstructural morphology within the enrichment domains.

4 ROVME for Thermo-mechanical Problems

ROVME was recently introduced to improve the computational efficiency of the VME approach [57]. In this manuscript, ROVME is generalized to address thermo-mechanical problems. Starting from the mechanical problem under temperature effect, we consider the following decomposition of the microscale displacement field:

$$\mathbf{u}_\alpha^m(\mathbf{x}, T, t) = \sum_{A=1}^{N_D} \mathbf{H}_A^\alpha(\mathbf{x}, T) \cdot \hat{\mathbf{u}}_A^{M\alpha}(T, t) + \int_{\Omega_\alpha} \mathbf{h}^\alpha(\mathbf{x}, \hat{\mathbf{x}}, T) : \boldsymbol{\varepsilon}^{vp}(\hat{\mathbf{x}}, T, t) \ d\hat{\mathbf{x}}$$

$$+\mathbf{G}^\alpha(\mathbf{x}, T)\,(T - T_0) \tag{21}$$

where, $\hat{\mathbf{u}}_A^{M\alpha}$ denotes the macroscale nodal coefficient of the enrichment domain, Ω_α; $\mathbf{H}_A^\alpha$, a second order tensor, is the influence function associated with the linear elastic component of the response field in Ω_α; $\mathbf{h}^\alpha$, a third order tensor, is the influence function for the inelastic deformation within the microstructure; and $\mathbf{G}^\alpha$, a first order tensor, is the influence function associated with the thermal expansion in the enrichment domain. The governing equations for the influence functions $\mathbf{H}_A^\alpha$, $\mathbf{h}^\alpha$ and $\mathbf{G}^\alpha$ are obtained from the microscale problem, Eq. (15). Substituting the constitutive equation, Eq. (2), and the microscale displacement field discretization, Eq. (21), into Eq. (15) yields ($\alpha = 1, 2, ...n_{\mathrm{en}}$):

$$\sum_{A=1}^{N_D} \int_{\Omega_\alpha} \nabla \mathbf{w}_\alpha^m : \mathbf{L}(T) : \left[\nabla \mathbf{H}_A^\alpha(T) + \nabla N_A\right] \ d\Omega \cdot \hat{\mathbf{u}}_A^{M\alpha}(T, t)$$

$$+ \int_{\Omega_\alpha} \nabla \mathbf{w}_\alpha^m : \mathbf{L}(T) : \left[\int_{\Omega_\alpha} \nabla \mathbf{h}^\alpha(\mathbf{x}, \hat{\mathbf{x}}, T) : \boldsymbol{\varepsilon}^{vp}(\hat{\mathbf{x}}, T, t) \ d\hat{\mathbf{x}} - \boldsymbol{\varepsilon}^{vp}(\mathbf{x}, T, t)\right] \ d\Omega$$

$$+ \int_{\Omega_\alpha} \nabla \mathbf{w}_\alpha^m : \mathbf{L}(T) \cdot \left[\mathbf{G}^\alpha(T)\,(T - T_0) - \boldsymbol{\alpha}^T\,(T - T_0)\right] \ d\Omega = 0 \tag{22}$$

We assume that each enrichment domain is sufficiently small compared to the macroscale structure and that the thermal gradient across an enrichment domain is negligible. A first order approximation is that the thermal state within the enrichment domain is spatially uniform, with enrichment domain temperature approximated as:

$$T^\alpha(t) = \frac{1}{|\Omega_\alpha|} \int_{\Omega_\alpha} T(\mathbf{x}, t) \ d\Omega \tag{23}$$

Considering the elastic state of the enrichment domain at uniform reference temperature,

T^α, and in the absence of inelastic processes, Eq. (22) reduces to:

$$\int_{\Omega_\alpha} \nabla \mathbf{w}_\alpha^m : \mathbf{L}(T^\alpha) : \nabla \mathbf{H}_A^\alpha(T^\alpha) \, d\Omega = -\int_{\Omega_\alpha} \nabla \mathbf{w}_\alpha^m : \mathbf{L}(T^\alpha) \cdot \nabla N_A \, d\Omega;$$
$$A = 1, 2, ..., N_D \tag{24}$$

Equation (24) is the elastic influence function problem, which is evaluated for $\mathbf{H}_A^\alpha(T^\alpha)$. Homogeneous Dirichlet boundary conditions are imposed to ensure that the microscale displacements vanish along $\partial\Omega_\alpha$ (see Eq. (13)). In the presence of inelastic deformation but at uniform reference temperature within the enrichment domain, the inelastic influence function problem in weak form is obtained:

$$\int_{\Omega_\alpha} \nabla \mathbf{w}_\alpha^m : \mathbf{L}(T^\alpha) : \nabla \mathbf{h}^\alpha(\mathbf{x}, \hat{\mathbf{x}}, T^\alpha) \, d\Omega = \int_{\Omega_\alpha} \nabla \mathbf{w}_\alpha^m : \mathbf{L}(T^\alpha) \, \delta^d(\mathbf{x} - \hat{\mathbf{x}}) \, d\Omega; \quad \forall \hat{\mathbf{x}} \in \Omega_\alpha \tag{25}$$

where, δ^d denotes the Dirac delta distribution. In the presence of thermal deformation and in view of Eqs. (24) and (25), Eq. (22) yields the thermal influence function problem:

$$\int_{\Omega_\alpha} \nabla \mathbf{w}_\alpha^m : \mathbf{L}(T^\alpha) \cdot \mathbf{G}^\alpha(T^\alpha) \, d\Omega = \int_{\Omega_\alpha} \nabla \mathbf{w}_\alpha^m : \mathbf{L}(T^\alpha) \cdot \boldsymbol{\alpha}^T \, d\Omega \tag{26}$$

The influence functions, $\mathbf{H}_A^\alpha$, $\mathbf{h}^\alpha$ and $\mathbf{G}^\alpha$, are temperature-dependent because the elastic properties of the constituents vary as a function of temperature (i.e., $\mathbf{L}(T^\alpha)$). For a fixed uniform temperature field, T^α, discrete approximations to the influence functions are evaluated numerically [4, 5, 42, 45].

4.1 Reduced basis for the microscale problem

The reduced basis is achieved through the following approximation of the stress and inelastic strain fields within an enrichment domain:

$$\boldsymbol{\sigma}(\mathbf{x}, T^\alpha, t) = \sum_{\gamma=1}^{NP_\alpha} N_\gamma^\alpha(\mathbf{x}) \, \boldsymbol{\sigma}_\gamma^\alpha(T^\alpha, t); \quad \boldsymbol{\varepsilon}^{vp}(\mathbf{x}, T^\alpha, t) = \sum_{\gamma=1}^{NP_\alpha} N_\gamma^\alpha(\mathbf{x}) \, \boldsymbol{\mu}_\gamma^\alpha(T^\alpha, t); \quad \mathbf{x} \in \Omega_\alpha \tag{27}$$

where, $\boldsymbol{\sigma}_\gamma^\alpha$ and $\boldsymbol{\mu}_\gamma^\alpha$ are the stress and inelastic strain coefficients, respectively. N_γ^α denotes reduced basis shape functions; and NP_α the order of the reduced basis. The reduced basis shape functions are taken to be piecewise constant over parts of the enrichment domain:

$$N_\gamma^\alpha(\mathbf{x}) = \begin{cases} 1, & \text{if } \mathbf{x} \in \Omega_\gamma^\alpha \\ 0, & \text{elsewhere} \end{cases} \tag{28}$$

9

where, $\{\Omega_\gamma^\alpha \mid \gamma = 1, 2, ..., NP_\alpha\}$ constitutes a non-overlapping partitioning of the enrichment domain. By this discretization, the stress and inelastic strain fields are approximated as piecewise constant over the enrichment domain.

Substituting the reduced order microscale partitioning (Eqs. (27) and (21)) into Eq. (2), the stress coefficient for an arbitrary part Ω_η^α within the enrichment domain Ω_α is expressed as:

$$\boldsymbol{\sigma}_\eta^\alpha(T^\alpha, t) = \sum_{A=1}^{N_D} \left[\mathbf{S}_{\eta A}^\alpha(T^\alpha) \cdot \hat{\mathbf{u}}_A^{M\alpha}(T^\alpha, t)\right] + \sum_{\gamma=1}^{NP_\alpha} \left[\mathbf{P}_{\eta\gamma}^\alpha(T^\alpha) : \boldsymbol{\mu}_\gamma^\alpha(T^\alpha, t)\right] \\ + \mathbf{Z}_\eta^\alpha(T^\alpha)\,(T^\alpha - T_0) \tag{29}$$

The homogenized coefficient tensors on each part Ω_η^α are:

$$\mathbf{S}_{\eta A}^\alpha(T^\alpha) = \frac{1}{|\Omega_\eta^\alpha|} \int_{\Omega_\eta^\alpha} \left[\mathbf{L}(\mathbf{x}, T^\alpha) \cdot \nabla N_A^\alpha(\mathbf{x}) + \mathbf{L}(\mathbf{x}, T^\alpha) : \nabla\mathbf{H}_A^\alpha(\mathbf{x}, T^\alpha)\right] \, d\Omega \tag{30}$$

$$\mathbf{P}_{\eta\gamma}^\alpha(T^\alpha) = \frac{1}{|\Omega_\eta^\alpha|} \int_{\Omega_\eta^\alpha} \left[\mathbf{L}(\mathbf{x}, T^\alpha) : \int_{\Omega_\gamma^\alpha} \nabla\mathbf{h}^\alpha(\mathbf{x}, \hat{\mathbf{x}}, T^\alpha) \, d\hat{\mathbf{x}} - \mathbf{L}(\mathbf{x}, T^\alpha)\,N_\gamma^\alpha(\mathbf{x})\right] \, d\Omega \tag{31}$$

$$\mathbf{Z}_\eta^\alpha(T^\alpha) = \frac{1}{|\Omega_\eta^\alpha|} \int_{\Omega_\eta^\alpha} \mathbf{L}(\mathbf{x}, T^\alpha) : \left[\nabla\mathbf{G}^\alpha(\mathbf{x}, T^\alpha) - \boldsymbol{\alpha}^T(\mathbf{x})\right] \, d\Omega \tag{32}$$

Since the homogenized coefficient tensors ($\mathbf{S}_{\eta A}^\alpha(T^\alpha)$, $\mathbf{P}_{\eta\gamma}^\alpha(T^\alpha)$ and $\mathbf{Z}_\eta^\alpha(T^\alpha)$) are obtained from the influence functions which always satisfy the microscale weak form equation, the stress coefficients computed using the coefficient tensors ensures that the reduced order microscale equilibrium state is satisfied for arbitrary macroscale displacement, inelastic strain coefficient, and temperature field over the enrichment domain.

In view of the linearity of the thermal problem, the microscale temperature field is expressed as:

$$T_\alpha^m(\mathbf{x}, t) = \sum_{A=1}^{N_D} \breve{H}_A^\alpha(\mathbf{x}) \cdot \hat{T}_A^{M\alpha}(t) \tag{33}$$

in which, $\breve{H}_A^\alpha$ is the temperature influence function evaluated by satisfying the microscale weak form, Eq. (20). The resulting temperature field is:

$$T(\mathbf{x}, t) = \sum_{A=1}^{N_D} \left[N_A(\mathbf{x}) + \breve{H}_A^\alpha(\mathbf{x})\right] \cdot \hat{T}_A^{M\alpha}(t) \tag{34}$$

The uniform temperature field within the enrichment domains (Eq. (23)) is evaluated using:

$$T^\alpha(t) = \sum_{A=1}^{N_D} \bar{H}_A^\alpha \, \hat{T}_A^{M\alpha}(t) \tag{35}$$

where,

$$\bar{H}_A^\alpha = \frac{1}{|\Omega_\alpha|} \int_{\Omega_\alpha} \nabla N_A^\alpha(\mathbf{x}) + \nabla \breve{H}_A^\alpha(\mathbf{x}) \; d\Omega \tag{36}$$

4.2 Approximation of Coefficient Tensors over Temperature

It is important to note that the influence functions and consequently the coefficient tensors
($\mathbf{S}_{\eta A}^\alpha$, $\mathbf{P}_{\eta\gamma}^\alpha$ and $\mathbf{Z}_\eta^\alpha$) are functions of temperature. Within a structural analysis subjected
to thermo-mechanical loads where temperature field is spatially and temporally varying, the
temperature-dependent coefficient tensors need to be stored separately for each enrichment
domain and updated at every increment. The update procedure requires the evaluation of the
influence function problems (Eqs. (24)-(26)) and the numerical integrations (Eqs. (30)-(32)),
both of which are computationally expensive. Instead, we consider the following approximation
of the temperature dependence of the coefficient tensors:

$$\mathbf{S}_{\eta A}^\alpha(T^\alpha) \approx \bar{\mathbf{S}}_{\eta A}^\alpha(T^\alpha; \mathbf{T}^{N_\alpha}) = \sum_{i=1}^{N_\alpha} \psi_i(T^\alpha) \; \hat{\mathbf{S}}_{\eta A i}^\alpha \tag{37}$$

$$\mathbf{P}_{\eta\gamma}^\alpha(T^\alpha) \approx \bar{\mathbf{P}}_{\eta\gamma}^\alpha(T^\alpha; \mathbf{T}^{N_\alpha}) = \sum_{i=1}^{N_\alpha} \psi_i(T^\alpha) \; \hat{\mathbf{P}}_{\eta\gamma i}^\alpha \tag{38}$$

$$\mathbf{Z}_\eta^\alpha(T^\alpha) \approx \bar{\mathbf{Z}}_\eta^\alpha(T^\alpha; \mathbf{T}^{N_\alpha}) = \sum_{i=1}^{N_\alpha} \psi_i(T^\alpha) \; \hat{\mathbf{Z}}_{\eta i}^\alpha \tag{39}$$

where, $\{\psi_i| \; i = 1, 2, ..., N_\alpha\}$ is a set of interpolation functions for the coefficient tensors. One
dimensional piecewise linear Lagrangian shape functions are employed in the current study.
N_α denotes the number of nodes in the temperature discretization ($\mathbf{T}^{N_\alpha}$) over a temperature
range:

$$\mathbf{T}^{N_\alpha} = \{T_1, T_2, ..., T_{N_\alpha}\}^T; \quad T_1 = T_{\min} \text{ and } T_{N_\alpha} = T_{\max} \tag{40}$$

where, $T_{\min}$ and $T_{\max}$ denote the minimum and maximum temperature that the structure is
subjected to, respectively. $\hat{\mathbf{S}}_{\eta A}^\alpha$, $\hat{\mathbf{P}}_{\eta\gamma}^\alpha$ and $\hat{\mathbf{Z}}_\eta^\alpha$ are the approximation bases for the corresponding
coefficient tensors such that:

$$\hat{\mathbf{S}}_{\eta A}^\alpha := \left\{\hat{\mathbf{S}}_{\eta A i}^\alpha = \mathbf{S}_{\eta A}^\alpha(T_i) \mid T_i \in \mathbf{T}^{N_\alpha}\right\}^T; \quad \hat{\mathbf{P}}_{\eta\gamma}^\alpha := \left\{\hat{\mathbf{P}}_{\eta\gamma i}^\alpha = \mathbf{P}_{\eta\gamma}^\alpha(T_i) \mid T_i \in \mathbf{T}^{N_\alpha}\right\}^T;$$
$$\hat{\mathbf{Z}}_\eta^\alpha := \left\{\hat{\mathbf{Z}}_{\eta i}^\alpha = \mathbf{Z}_\eta^\alpha(T_i) \mid T_i \in \mathbf{T}^{N_\alpha}\right\}^T \tag{41}$$

For an arbitrary microstructure, the coefficient tensors for each temperature in $\mathbf{T}^{N_\alpha}$ are eval-
uated a-priori and stored for the approximation.

4.3 Identification of the temperature approximation basis

The accuracy of the approximation stated in Eqs. (37) - (39) directly depends on proper identification of $\mathbf{T}^{N_\alpha}$, which in turn depends on the variation of the elastic properties of each microstructural constituent as a function of temperature. The optimum $\mathbf{T}^{N_\alpha}$ should contain the smallest number of basis nodes that confine the error between the directly computed (Eqs. (30)-(32)) and the approximated (Eqs. (37)-(39)) coefficient tensors. Consequently, the identification of the approximation basis is posed as an optimization problem. We seek to find the optimal basis node set $(\mathbf{T}_{\text{opt}}^{N_\alpha^*})$ for fixed N_α^*, such that

$$
E_r(N_\alpha{}^*) = \min_{\mathbf{T}^{N_\alpha^*}} \left\{ \max \left[\left\| \mathbf{S}_{\eta A}(T^\alpha) - \bar{\mathbf{S}}_{\eta A}(T^\alpha; \mathbf{T}^{N_\alpha^*}) \right\|_\infty \right. \right.
$$

$$
\left. \left. \left\| \mathbf{P}_{\eta\gamma}(T^\alpha) - \bar{\mathbf{P}}_{\eta\gamma}(T^\alpha; \mathbf{T}^{N_\alpha^*}) \right\|_\infty , \left\| \mathbf{Z}_\eta(T^\alpha) - \bar{\mathbf{Z}}_\eta(T^\alpha; \mathbf{T}^{N_\alpha^*}) \right\|_\infty \right] \right\}; \tag{42}
$$

$$
\forall\ \eta, \gamma = 1, 2, ..., NP_\alpha \text{ and } A = 1, 2, ..., N_D;\ \ T^\alpha \in [T_{\min}, T_{\max}]
$$

It is trivial to observe that the error (E_r) is non-increasing with N_α^*, e.g., $E_r(N_\alpha{}^*) \geq E_r(N_\alpha{}^* + 1)$. The optimal basis order is then the smallest N_α^*, such that

$$
E_r(N_\alpha) \leq TOL \tag{43}
$$

and the corresponding basis set is $\mathbf{T}^{N_\alpha}$. TOL denotes the tolerance. It is possible to evaluate Eq. (42) using traditional optimization methods. In order to reduce the computational cost associated with solving influence function problems at each iteration of the optimization operation, an alternative of Eq. (42) is used:

$$
E_r(N_\alpha{}^*) = \min_{\mathbf{T}^{N_\alpha^*}} \left\{ \left\| \mathbf{L}_\eta(T^\alpha) - \bar{\mathbf{L}}_\eta \right\|_\infty \right\}; \quad \forall\ \eta = 1, 2, ..., NP_\alpha \tag{44}
$$

where, $\mathbf{L}_\eta$ is the temperature-dependent tensor of elastic moduli and $\bar{\mathbf{L}}_\eta$ is its discrete approximation. Equations (44) and (43) are numerically evaluated for the optimum $\mathbf{T}^{N_\alpha}$ using the adaptive approximation method [49, 50].

To further illustrate the procedure stated above, we consider an example for a SiC/Ti-6242s composite material [8, 9, 6, 13]. The microstructure of the SiC/Ti-6242s composite is shown in Fig. 2(a). The silicon carbide fiber (SiC) is assumed to be temperature-independent and isotropic, with Young's modulus and Poison's ratio of 395 GPa and 0.25, respectively. The Young's modulus of the matrix material (Ti-6242s) is taken to be temperature-dependent, as shown in Fig. 2(b) [52]. The Poison's ratio of the matrix is taken as temperature-independent, $\nu=0.32$. Through adaptive approximation with 10$^\text{o}$C as the minimum partition interval, the
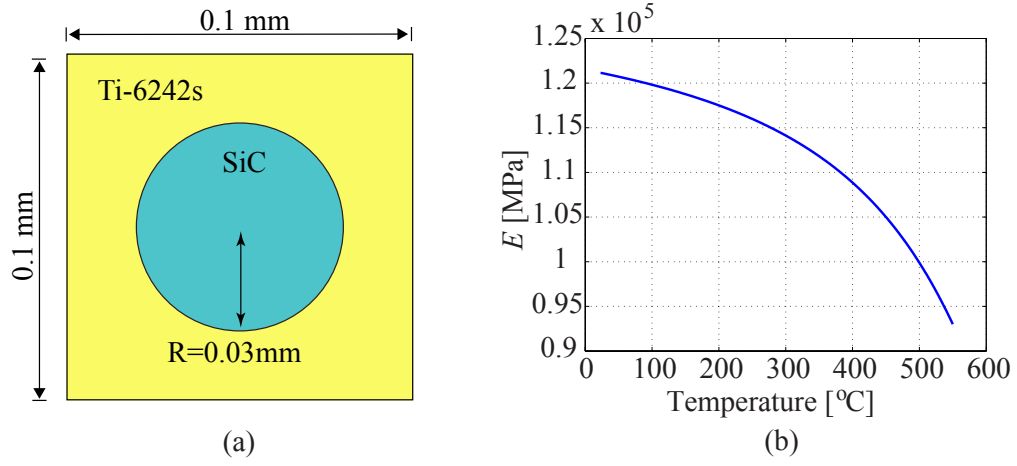
Figure 2: (a) Microstructure of the SiC/Ti-6242s composite; and (b) temperature dependence of Young's modulus for the Ti-6242s matrix.
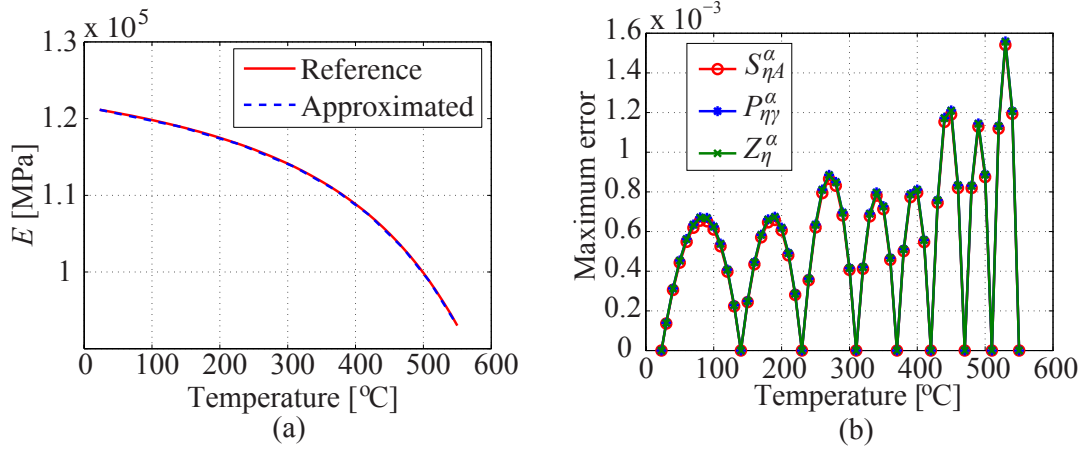

Figure 3: Performance of determined temperature basis for : (a) approximated Young's modulus of Ti-6242s; and (b) maximum errors in the approximated coefficient tensors.

optimum temperature approximation basis is determined as $\mathbf{T}^{N_\alpha} = \{23, 140, 230, 310, 370, 420, 470, 510, 550\}$. It contains 9 temperature nodes and the approximated Young's modulus function is plotted in Fig. 3(a). The tolerance employed is 0.003 in the current example. Using the determined $\mathbf{T}^{N_\alpha}$, the maximum errors between the approximated and directly computed coefficient tensors are presented in Fig 3(b).

5   Computational Implementation

This section provides the numerical implementation of the ROVME method for thermo-mechanical problems, along with an implementation strategy. The implementation of the direct VME method for mechanical problems under temperature effect (employed in the verification of the ROVME method) is listed in the Appendix. The thermal and mechanical problems are evaluated incrementally in a staggered fashion, since the two problems include one-way coupling only (i.e., effect of temperature on mechanical response). The coupled temperature and mechanical response fields are solved separately, through separation of variables. With the assumption that the enrichment domains are sufficiently small, the uniform temperature field (T^α) of each enrichment domain (Ω_α) is obtained by homogenizing the temperature field of the enriched macroscale element.

Considering a discrete set of instances with the observation period ($\{0, {}_1t, {}_2t, ..., {}_nt, {}_{n+1}t, ..., t_e\}$) and taking the temperature field as a known variable at each time step, the elasto-viscoplastic mechanical problem under temperature effect is numerically assessed through a Newton-Raphson iterative scheme summarized below. For simplicity of the presentation, the superscript, α, has been omitted from the response variable in the implementation described below.

5.1   ROVME formulation in an arbitrary enrichment domain

The rate-form constitutive equation for an arbitrary part, Ω_η^α, is obtained by taking the time derivative of Eq. (29):

$$
\begin{aligned}
\dot{\boldsymbol{\sigma}}_\eta(t) = {} & \sum_{A=1}^{N_D} \left[\mathbf{S}_{\eta A}(T) \cdot \dot{\hat{\mathbf{u}}}_A^M(T, t) \right] + \sum_{\gamma=1}^{NP} \left[\mathbf{P}_{\eta\gamma}(T) : \dot{\boldsymbol{\mu}}_\gamma(T, t) \right] + \mathbf{Z}_\eta(T)\, \dot{T} \\
& + \sum_{A=1}^{N_D} \left[\frac{\partial \mathbf{S}_{\eta A}(T)}{\partial T} \dot{T} \cdot \hat{\mathbf{u}}_A^M(T, t) \right] + \sum_{\gamma=1}^{NP} \left[\frac{\partial \mathbf{P}_{\eta\gamma}(T)}{\partial T} \dot{T} : \boldsymbol{\mu}_\gamma(T, t) \right] + \frac{\partial \mathbf{Z}_\eta(T)}{\partial T}\, \dot{T}(T - T_0)
\end{aligned}
\tag{45}
$$

The viscoplastic slip evolution of the ROVME method for each part Ω_γ^α in the enrichment domain is discretized by a one-parameter family (θ-rule):

$$
\dot{\boldsymbol{\mu}}_\gamma(t) = (1 - \theta)\, \dot{\boldsymbol{\mu}}_\gamma(\mathbf{x}, {}_nt) + \theta\, \dot{\boldsymbol{\mu}}_\gamma(\mathbf{x}, {}_{n+1}t); \quad t \in [{}_nt,\ {}_{n+1}t]
\tag{46}
$$

where, $\theta \in [0, 1]$ is an algorithmic parameter. Performing time discretization of Eq. (45) with Eq. (46), the residual of the constitutive equation for an arbitrary part Ω_η^α yields:

$$
\begin{aligned}
\mathbf{R}_\eta \equiv\ & _{n+1}\boldsymbol{\sigma}_\eta - {_n}\boldsymbol{\sigma}_\eta - \sum_{A=1}^{N_D} {_{n+1}}\mathbf{S}_{\eta A} \cdot \left({_{n+1}}\hat{\mathbf{u}}_A^M - {_n}\hat{\mathbf{u}}_A^M \right) - (1 - \theta)\ \Delta t \sum_{\gamma=1}^{NP} {_{n+1}}\mathbf{P}_{\eta\gamma} : {_n}\dot{\boldsymbol{\mu}}_\gamma \\
& - \theta\ \Delta t \sum_{\gamma=1}^{NP} {_{n+1}}\mathbf{P}_{\eta\gamma} : {_{n+1}}\dot{\boldsymbol{\mu}}_\gamma - {_n}\mathbf{Z}_\eta\ \left({_{n+1}}T - {_n}T \right) \\
& - \sum_{A=1}^{N_D} {_{n+1}}\left(\frac{\partial \mathbf{S}_{\eta A}}{\partial T} \right) \cdot {_{n+1}}\hat{\mathbf{u}}_A^M\ \left({_{n+1}}T - {_n}T \right) - \sum_{\gamma=1}^{NP} {_{n+1}}\left(\frac{\partial \mathbf{P}_{\eta\gamma}}{\partial T} \right) :\ {_{n+1}}\boldsymbol{\mu}_\gamma\ \left({_{n+1}}T - {_n}T \right) \\
& - {_{n+1}}\left(\frac{\partial \mathbf{Z}_\eta}{\partial T} \right)\ \left({_{n+1}}T - {_n}T \right) \left({_{n+1}}T - T_0 \right) = 0
\end{aligned}
\tag{47}
$$

in which, the left subscript n and $n + 1$ denote the value of a field variable at $_n t$ and $_{n+1}t$, respectively. The equilibrium states and response fields of the nonlinear system at $_n t$ is the "known" configuration. The temperature field $(_{n+1}T)$ and the coefficient tensors $(_{n+1}\mathbf{S}_{\eta A},\ _{n+1}\mathbf{P}_{\eta\gamma},\ _{n+1}\mathbf{Z}_\eta)$ are known at $_{n+1}t$. The temperature derivatives of the coefficient tensors $_{n+1}(\partial \mathbf{S}_{\eta A}/\partial T)$, $_{n+1}(\partial \mathbf{P}_{\eta\gamma}/\partial T)$ and $_{n+1}(\partial \mathbf{Z}_\eta/\partial T)$ are assessed numerically. In the remainder of this section, the left subscript $n + 1$ of the fields at the current time step is omitted for simplicity of the presentation. Forming a Newton iteration through a first order Taylor series approximation of Eq. (47), the residual of the stress-strain equation yields:

$$
\begin{aligned}
\mathbf{R}_\eta^{k+1} \approx\ & \mathbf{R}_\eta^k + \sum_{\gamma=1}^{NP} \left[\left(\delta_{\eta\gamma}^K\ \mathbf{I} - \theta\ \Delta t\ \mathbf{P}_{\eta\gamma} : \mathbf{C}_\gamma^k \right) : \delta \boldsymbol{\sigma}_\gamma \right] - \sum_{\gamma=1}^{NP} \left(\theta\ \Delta t\ \mathbf{P}_{\eta\gamma} : \mathbf{G}_\gamma^k + \mathbf{D}_{\eta\gamma} \right) : \delta \boldsymbol{\mu}_\gamma \\
& - \sum_{A=1}^{N_D} \left(\tilde{\mathbf{S}}_{\eta A} \cdot \delta \hat{\mathbf{u}}_A^M \right) = 0
\end{aligned}
\tag{48}
$$

where, superscript k is the Newton iteration count; $\delta(\cdot)$ indicates the increment of the response field $(\cdot)$ during the current iteration (i.e., $\delta(\cdot) = (\cdot)^{k+1} - (\cdot)^k$); $\delta_{\eta\gamma}^K$ the Kronecker delta; $\mathbf{I}$ the fourth order identity tensor; and

$$
\mathbf{D}_{\eta\gamma} = \left(\frac{\partial \mathbf{P}_{\eta\gamma}}{\partial T} \right) (T - {_n}T)\,; \quad \tilde{\mathbf{S}}_{\eta A} = \mathbf{S}_{\eta A} + \left(\frac{\partial \mathbf{S}_{\eta A}}{\partial T} \right) (T - {_n}T)
\tag{49}
$$

The operators $\mathbf{C}_\gamma^k$ and $\mathbf{G}_\gamma^k$ are defined as:

$$
\mathbf{C}_\gamma^k = \left(\frac{\partial \dot{\boldsymbol{\mu}}_\gamma}{\partial \boldsymbol{\sigma}_\gamma} \right)^k\,; \quad \mathbf{G}_\gamma^k = \left(\frac{\partial \dot{\boldsymbol{\mu}}_\gamma}{\partial \boldsymbol{\mu}_\gamma} \right)^k
\tag{50}
$$

The explicit expressions for $\mathbf{C}_\gamma^k$ and $\mathbf{G}_\gamma^k$ are described in Ref. [57]. Taylor series approximation does not include the derivative with respect to the temperature field, since it is taken as a known variable for the mechanical problem. The residual of the kinematic equation (Eq. (46)) for an arbitrary part Ω_γ^α is defined as:

$$\boldsymbol{\lambda}_\gamma \equiv \boldsymbol{\mu}_\gamma - {}_n\boldsymbol{\mu}_\gamma - \Delta t \,(1-\theta)\,{}_n\dot{\boldsymbol{\mu}}_\gamma - \Delta t\,\theta\,\dot{\boldsymbol{\mu}}_\gamma = 0 \tag{51}$$

Performing a first order Taylor series approximation of Eq. (51), the inelastic coefficient increment at the current Newton iteration is expressed as:

$$\delta\boldsymbol{\mu}_\gamma = \left(\mathbf{I} - \theta\,\Delta t\,\mathbf{G}_\gamma^k\right)^{-1} : \left(\theta\,\Delta t\,\mathbf{C}_\gamma^k\right) : \delta\boldsymbol{\sigma}_\gamma - \left(\mathbf{I} - \theta\,\Delta t\,\mathbf{G}_\gamma^k\right)^{-1} : \boldsymbol{\lambda}_\gamma^k \tag{52}$$

Substituting Eq. (52) into Eq. (48), the inelastic coefficients are condensed out to yield:

$$\sum_{\gamma=1}^{NP}\left(\mathbf{Q}_{\eta\gamma}^k : \delta\boldsymbol{\sigma}_\gamma\right) = \sum_{A=1}^{N_D}\left(\tilde{\mathbf{S}}_{\eta A} : \delta\hat{\mathbf{u}}_A^M\right) - \mathbf{V}_\eta^k \tag{53}$$

where, $\mathbf{Q}_{\eta\gamma}^k$ and $\mathbf{V}_\eta^k$ are defined as:

$$\begin{aligned}
\mathbf{Q}_{\eta\gamma}^k = {}&\delta_{\eta\gamma}^K\,\mathbf{I} - \theta\,\Delta t\,\mathbf{P}_{\eta\gamma} : \mathbf{C}_\gamma^k \\
&- \theta\,\Delta t\,\left(\theta\,\Delta t\,\mathbf{P}_{\eta\gamma} : \mathbf{G}_\gamma^k + \mathbf{D}_{\eta\gamma}\right) : \left(\mathbf{I} - \theta\,\Delta t\,\mathbf{G}_\gamma^k\right)^{-1} : \mathbf{C}_\gamma^k
\end{aligned} \tag{54}$$

$$\mathbf{V}_\eta^k = \mathbf{R}_\eta^k + \sum_{\gamma=1}^{NP}\left(\theta\,\Delta t\,\mathbf{P}_{\eta\gamma} : \mathbf{G}_\gamma^k + \mathbf{D}_{\eta\gamma}\right) : \left(\mathbf{I} - \theta\,\Delta t\,\mathbf{G}_\gamma^k\right)^{-1} : \boldsymbol{\lambda}_\gamma^k \tag{55}$$

Considering the stress increment over each part of the enrichment domain ($\eta = 1, 2, ..., NP$) in Eq. (53) separately, the stress increment vector for the enrichment domain is obtained as:

$$\delta\boldsymbol{\sigma} = \left(\mathbf{Q}^k\right)^{-1}\mathbf{S}\,\delta\hat{\mathbf{u}}^M - \left(\mathbf{Q}^k\right)^{-1}\mathbf{V}^k \tag{56}$$

in which, the coefficient tensors $\mathbf{Q}^k$ and $\mathbf{S}$ are defined as:

$$\mathbf{Q}^k = \left[\mathbf{Q}_{\eta\gamma}^k\right]_{\eta,\gamma\in[1,NP]}; \qquad \mathbf{S} = \left[\tilde{\mathbf{S}}_{\eta A}\right]_{\eta\in[1,NP], A\in[1,N_D]} \tag{57}$$

and

$$\delta\boldsymbol{\sigma} = \left\{ \left(\delta\boldsymbol{\sigma}_1^{k+1}\right)^{\mathrm{T}} \left(\delta\boldsymbol{\sigma}_2^{k+1}\right)^{\mathrm{T}}, ..., \left(\delta\boldsymbol{\sigma}_{NP}^{k+1}\right)^{\mathrm{T}} \right\}^{\mathrm{T}} \tag{58a}$$

$$\delta\hat{\mathbf{u}}^M = \left\{ \left(\delta\hat{\mathbf{u}}_1^{M,k+1}\right)^{\mathrm{T}}, \left(\delta\hat{\mathbf{u}}_2^{M,k+1}\right)^{\mathrm{T}}, ..., \left(\delta\hat{\mathbf{u}}_{N_D}^{M,k+1}\right)^{\mathrm{T}} \right\}^{\mathrm{T}} \tag{58b}$$

$$\mathbf{V}^k = \left\{ \left(\mathbf{V}_1^k\right)^{\mathrm{T}}, \left(\mathbf{V}_2^k\right)^{\mathrm{T}}, ..., \left(\mathbf{V}_{NP}^k\right)^{\mathrm{T}} \right\}^{\mathrm{T}} \tag{58c}$$

Correspondingly, the vector-matrix form of the weak form residual of the enrichment domain at the current iteration $(k+1)$ yields:

$$\tilde{\boldsymbol{\Psi}}^{M,k+1} = \mathbf{K}\,\delta\hat{\mathbf{u}}^M - \delta\mathbf{f} \tag{59}$$

where,

$$\mathbf{K} = (\mathbf{B})^{\mathrm{T}} \left(\mathbf{Q}^k\right)^{-1} \mathbf{S} \tag{60}$$

$$\delta\mathbf{f} = (\mathbf{B})^{\mathrm{T}} \left(\mathbf{Q}^k\right)^{-1} \mathbf{V}^k - \tilde{\boldsymbol{\Psi}}^{M,k} + \tilde{\boldsymbol{\Psi}}^{MT} \tag{61}$$

$$\mathbf{B} = \left[\int_{\Omega_\gamma^\alpha} \nabla N_A \, d\Omega \, \hat{\mathbf{w}}_A^M \right]_{\gamma \in [1,NP], \ A \in [1,N_D]} \tag{62}$$

$$\tilde{\boldsymbol{\Psi}}^{MT} = \left[\int_{\Gamma^t} N_A \, \tilde{\mathbf{t}} \, d\Gamma \, \hat{\mathbf{w}}_A^M \right]_{A \in [1,N_D]} \tag{63}$$

The linearized reduced order macroscale weak form (Eq. (59)) is solved incrementally until convergence is satisfied.

5.2   ROVME implementation algorithm

The implementation of the formulation is performed using the commercial software package, Diffpack [24], in C++ computer language. The overall implementation strategy is summarized in Fig. 4, where the microscale superscript (α) and part subscript (γ) are omitted for clarity. In the preprocessing phase prior to the simulation, the coefficient tensors $(\mathbf{S}_{\eta A}(T)$, $\mathbf{P}_{\eta\gamma}(T)$ and $\mathbf{Z}_\eta(T))$ at each temperature in $\mathbf{T}^N$ are computed using Eqs. (30), (31), (32) and stored $(A = 1, 2, ..., N_D; \gamma$ and $\eta = 1, 2, ..., NP)$ for each enrichment domain. The temperature influence function $(\breve{H}_A^\alpha)$ and the homogenization tensor $(\bar{H}_A^\alpha)$ are also evaluated and stored for each enrichment domain $(A = 1, 2, ..., N_D)$. At an arbitrary time $_nt$, the system is in equilibrium with the constitutive relations satisfied for the problem domain. The algorithm seeks to find the equilibrium state at $_{n+1}t$ as follows:
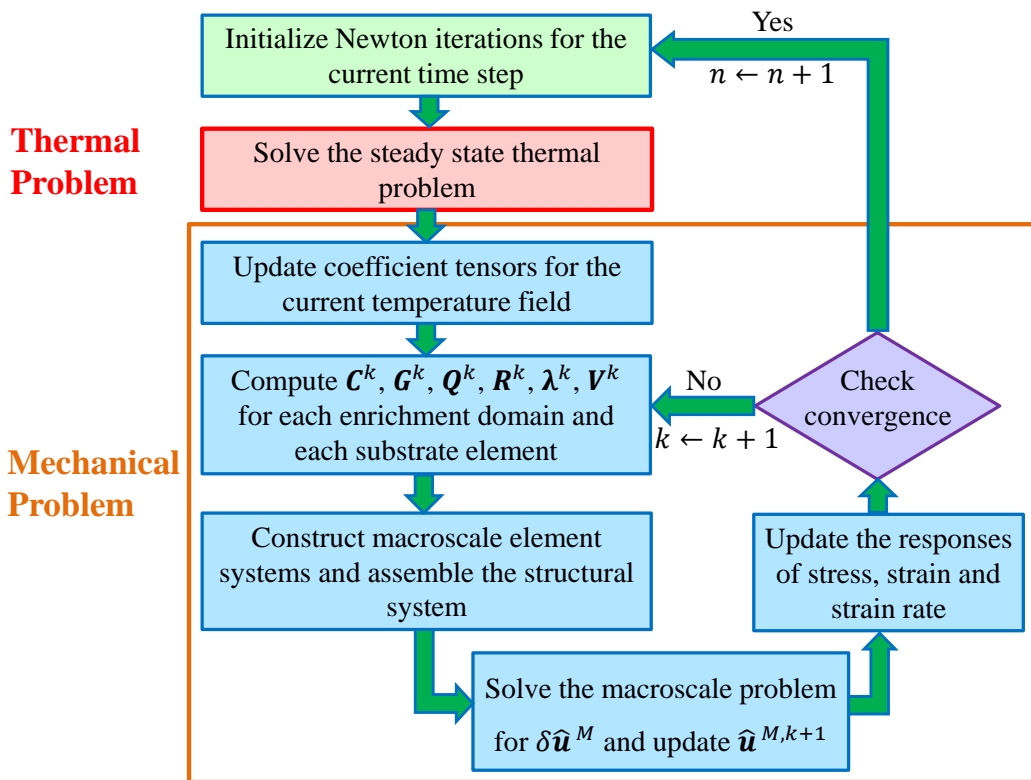
17

Figure 4: Reduced order variational multiscale enrichment implementation strategy (the subscripts , γ and η, indicating parts in enrichment domains are omitted for clarity).

Given: $_{n}\hat{\mathbf{u}}^{M}, _{n}\boldsymbol{\sigma}, _{n}\boldsymbol{\varepsilon}^{vp}$ and $_{n}\dot{\boldsymbol{\varepsilon}}^{vp}$ ($_{n}\boldsymbol{\mu}_{\gamma}$ and $_{n}\dot{\boldsymbol{\mu}}_{\gamma}$ for enrichment domains) at time $_{n}t$.

Find: $\hat{\mathbf{u}}^{M}, \boldsymbol{\sigma}, \boldsymbol{\varepsilon}^{vp}$ and $\dot{\boldsymbol{\varepsilon}}^{vp}$ ($\boldsymbol{\mu}_{\gamma}$ and $\dot{\boldsymbol{\mu}}_{\gamma}$ for enrichment domains) at time $_{n+1}t$.

1. Initialize by setting: $k=0$, $\hat{\mathbf{u}}^{M,0} = {}_{n}\hat{\mathbf{u}}^{M}$, $\boldsymbol{\sigma}^{0} = {}_{n}\boldsymbol{\sigma}$, $\boldsymbol{\varepsilon}^{vp,0} = {}_{n}\boldsymbol{\varepsilon}^{vp}$, and $\dot{\boldsymbol{\varepsilon}}^{vp,0} = {}_{n}\dot{\boldsymbol{\varepsilon}}^{vp}$ ($\boldsymbol{\mu}_{\gamma}^{0} = {}_{n}\boldsymbol{\mu}_{\gamma}$, and $\dot{\boldsymbol{\mu}}_{\gamma}^{0} = {}_{n}\dot{\boldsymbol{\mu}}_{\gamma}$ for enrichment domains).

2. Solve the steady state thermal problem for the current time, and for each enrichment domain (Ω_{α}, $\alpha = 1, 2, ..., n_{\text{en}}$):

   (1) Homogenize the temperature field over the enrichment domain (Eq. (35)).

   (2) Update the coefficient tensors ($\mathbf{S}_{\eta A}(T)$, $\mathbf{P}_{\eta\gamma}(T)$ and $\mathbf{Z}_{\eta}(T)$) using Eqs. (37)-(39).

   (3) Evaluate $\mathbf{D}_{\eta\gamma}$ and $\tilde{\mathbf{S}}_{\eta A}$ from Eq. (49) and assemble $\mathbf{S}$ using Eq. (57).

3. Loop over all enrichment domains:

   (1) Compute $\mathbf{C}_{\gamma}^{k}$, $\mathbf{G}_{\gamma}^{k}$, $\mathbf{Q}_{\eta\gamma}^{k}$, $\mathbf{R}_{\eta}^{k}$, $\boldsymbol{\lambda}_{\eta}^{k}$, $\mathbf{V}_{\eta}^{k}$, $\mathbf{Q}^{k}$ and $\mathbf{V}^{k}$ from Eqs. (50), (54), (47), (51), (55), (57) and (58c) .

   (2) Construct $\mathbf{K}$ and $\delta\mathbf{f}$ for the current enrichment domain using Eqs. (60) and (61).

4. Following the standard finite element procedure, construct the macroscale elementary stiffnesses for the substrate elements and assemble the macroscale system.

5. Solve the macroscale problem for $\delta\hat{\mathbf{u}}^{M}$ and update the macroscale displacement field ($\hat{\mathbf{u}}^{M,k+1} = \hat{\mathbf{u}}^{M,k} + \delta\hat{\mathbf{u}}^{M}$).

6. Loop over all enrichment domains:

   (1) Determine the stress coefficient increment $\delta\boldsymbol{\sigma}$ (Eq. (56)) and update the stress coefficient $\boldsymbol{\sigma}^{k+1} = \boldsymbol{\sigma}^{k} + \delta\boldsymbol{\sigma}$.

   (2) Evaluate the inelastic strain coefficient increment $\delta\boldsymbol{\mu}_{\gamma}$ (Eq. (52)) and update the inelastic strain coefficient $\boldsymbol{\mu}_{\gamma}^{k+1} = \boldsymbol{\mu}_{\gamma}^{k} + \delta\boldsymbol{\mu}_{\gamma}$.

   (3) Compute the inelastic strain rate coefficient $\dot{\boldsymbol{\mu}}_{\gamma}$ using the evolution equation of the material.

7. Loop over all substrate elements to update stress ($\boldsymbol{\sigma}^{k+1}$), strain ($\boldsymbol{\varepsilon}^{vp,k+1}$) and strain rate ($\dot{\boldsymbol{\varepsilon}}^{vp,k+1}$) using classical response update procedures [56].

8. Check for convergence:

$$\mathrm{e}^{M} = \frac{\|\hat{\mathbf{u}}^{M,k+1} - \hat{\mathbf{u}}^{M,k}\|_{2}}{\|\hat{\mathbf{u}}^{M,k+1} - {}_{n}\hat{\mathbf{u}}^{M}\|_{2}} \leq \text{Convergence tolerance} \tag{64}$$

9. If convergence is not satisfied, set iteration counter $k \leftarrow k+1$ and proceed with the next iteration.

19

Table 1: Materials parameters for phase II material in the microstructure.

Property	E_0 [GPa] [1]	ν	A [MPa]	B [MPa]	m	n
Value	120.8	0.32	895	125	0.85	0.2
Property	T_{room} [°C]	T_{melt} [°C]	γ [MPa/second]	q	α^T [1/°C]	k [W/mK]
Value	23	1700	25	1.0	7.7×10^{-6}	20

6   Numerical Verification

The verifications of the ROVME method particularly focus on the coupling effects in the thermo-mechanical behavior. The accuracy characteristics of the ROVME method is assessed by comparing the results with the direct VME approach, as well as with the single scale finite element method (FEM), in which the heterogeneous microstructure is resolved within the enrichment region. A two-phase particulate composite with circular inclusions is employed (Fig. 2(a)). Phase I is the silicon carbide constituent, taken to be elastic with Young's modulus (E) of 395 GPa, Poisson's ratio (ν) of 0.25, the thermal expansion coefficient (α) of 4.2×10^{-6}/°C and the thermal conductivity (k) of 120 W/mK [12, 13]. Phase II is Ti-6242s, taken to be elasto-viscoplastic [23, 46]. The flow stress is expressed using the modified Johnson-Cook model [22, 43]:

$$\sigma_y = [A + B(\bar{\varepsilon}^{vp})^n] [1 - (T^*)^m] \tag{65}$$

where, A, B, n and m are material parameters; $\bar{\varepsilon}^{vp}$ the effective viscoplastic strain and T^* is the non-dimensional temperature:

$$T^* = \frac{T - T_{\text{room}}}{T_{\text{melt}} - T_{\text{room}}} \tag{66}$$

where, T_{room} and T_{melt} are the room and melting temperatures, respectively. Instead of incorporating the strain rate term directly as in the standard Johnson-Cook model, the strain rate effect is modeled through the Perzyna formulation [56, 57]. The values of the parameters for Ti-6242s are shown in Table 1, in which γ is the fluidity parameter and q is the viscoelastic hardening parameter. The Young's modulus of Ti-6242s is taken to vary as a function of temperature as shown in Fig. 2(b). Phase III denotes the homogenized composite used in the substrate region, the properties of which are computed using the rule of mixtures and taken to remain elastic [8, 6]. The Young's modulus of Phase III at the room temperature is 170 GPa and linearly drops to 140 GPa at 550°C. The Poisson's ratio is 0.3. The thermal expansion coefficient is 5.0×10^{-6}/°C and the thermal conductivity is 48 W/mK.

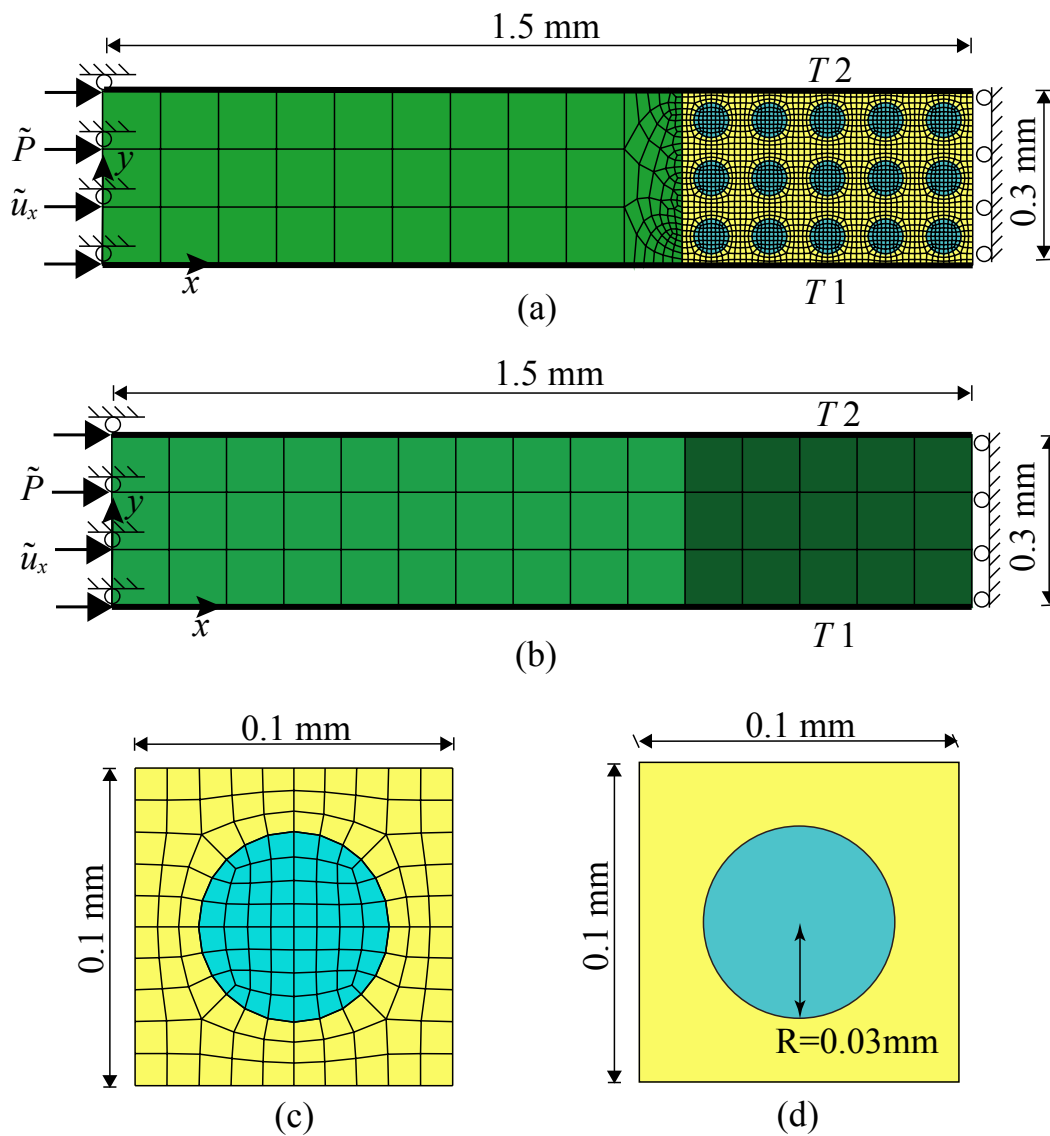[1]E_0 denotes the Young's modulus at the room temperature.

Figure 5: Model sketch and discretization of: (a) finite element method; (b) macroscale problem of the VME and ROVME methods; (c) microscale problem of the VME method; and (d) microscale problem of the ROVME method with 2 parts.
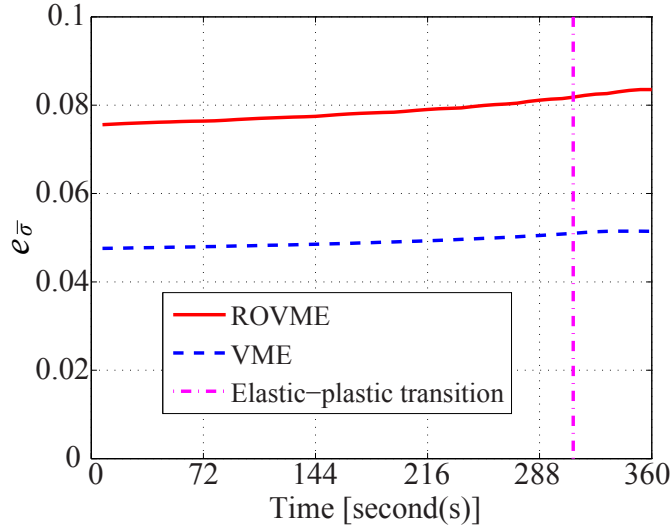
Figure 6: Errors in equivalent stress for specimen with uniform temperature field.

A 2-D plane strain, 3 mm × 0.3mm, composite beam is considered. Due to symmetry, only half of the beam is discretized. The ratio between the size of the enrichment domain and the size of the critical subregion is 1/5. The macro- and microscale discretization for the ROVME and VME models are shown in Fig. 5, along with the reference finite element discretization. The macroscale discretization, Fig. 5(b), contains 64 nodes and 45 quadrilateral finite elements. The enrichment region contains 15 macroscale elements, and is positioned close to the center of the beam since the center of the beam has the largest deformation and stress state under the applied loads. Each of the enrichment domains contains a phase I inclusion at the center, and a phase II matrix. The particle volume fraction is 28.3% [8, 6, 13]. The ROVME model of the enrichment domain (Fig. 5(d)) consists of 2 parts that corresponds to the domains of the constituents, and 6 degrees of freedom (DOFs). Each VME microstructure (Fig. 5(c)) is discretized using 148 quadrilateral elements and 338 DOFs. The corresponding direct finite element mesh (Fig. 5(a)) contains 2,340 quadrilateral elements and 4,844 DOFs. The temperatures in $\mathbf{T}^{N_\alpha}$ as determined in Section 4.3 is employed for the approximation of the ROVME coefficient tensors.

6.1   Specimen subjected to uniform temperature field

The first specimen is confined at both ends (i.e., $\tilde{u}_x = 0$ and $\tilde{P} = 0$ in Fig. 5(a) and (b)) subjected to uniform temperature field that monotonically increases from 23ºC to 550ºC in 6 minutes. The mechanical deformation of the specimen is therefore induced by the thermal expansions only. The time step size is set to 0.72 second. Further reduction in the time step size does not significantly improve the results. To investigate the performance of the ROVME

22

and VME models compared with the reference model, the stress error over the enrichment region at an arbitrary time, t, is computed:

$$e_{\bar{\sigma}}(t) = \frac{\sum\limits_{\alpha=1}^{n_{\text{en}}} \sum\limits_{\gamma=1}^{NP_\alpha} \left\| \bar{\sigma}_\gamma^{\text{FEM}}(t) - \bar{\sigma}_\gamma(t) \right\|_{2,\Omega_\gamma^\alpha}}{\sum\limits_{\alpha=1}^{n_{\text{en}}} \sum\limits_{\gamma=1}^{NP_\alpha} \left\| \bar{\sigma}_\gamma^{\text{FEM}}(t) \right\|_{2,\Omega_\gamma^\alpha}} \tag{67}$$

where, $\bar{\sigma}_\gamma^{\text{FEM}}$ and $\bar{\sigma}_\gamma$ denote the homogenized equivalent stress over part, Ω_γ^α, obtained from the direct finite element method and the model being assessed (VME or ROVME), respectively. $\|\cdot\|_{2,\Omega_\gamma^\alpha}$ is the L_2 norm of the response field computed over Ω_γ^α. The equivalent stress errors for the ROVME and direct VME methods are shown in Fig. 6 as a function of time. Until temperature reaches 477°C ($t = 310$ seconds), the structure deforms elastically. Further heating causes plastic deformation as marked by the elastic-plastic transition line in Fig. 6. The maximum errors occur at the end of the simulation, and are less than 8.4% and 5.2% for the ROVME and VME models, respectively. The primary cause of the errors in the VME model is the microscale boundary condition, which leads to more rigid reactions than the reference model. The ROVME model displays slightly higher errors primarily due to the kinematic constraints imposed by Eq. (27). The slight increase in error as a function of time within the elastic loading stage is attributed to the increase in the stiffness contrast between the inclusion and the matrix as a function of temperature. Larger stiffness contrast leads to slightly higher errors as demonstrated in Ref. [57].

Figure 7 presents the equivalent stress contours of the structure at the end of the simulation predicted by the reference, VME and ROVME models. The stress contours of the VME and ROVME models are obtained by embedding the response of each enrichment domain into the coarse response field at post-processing. The stress contours computed by the VME and the ROVME approaches show slightly stiffer response compared with the reference solution due to constrained kinematics, but are able to capture the local and global stress distributions with reasonable accuracy. The equivalent stress over the line at the center of the enrichment region (x=1.0-1.5 mm, y=0.15 mm in Fig. 5 (a) and (b)) is plotted for all of the models, as shown in Fig. 8. Although the peak values of the ROVME model are closer to the results of the reference solution, the direct VME model generally follows the stress variation of the reference model more closely. Since the stress is taken to be constant over each part, the ROVME method does not resolve the stress variation around the inter-enrichment domain interfaces. The computational cost for the ROVME simulation is 5.58 minutes while for the finite element simulation is 63.8 minutes. The ROVME is 11.43 times faster than the reference model for the current example, which demonstrates the efficiency of the proposed method.
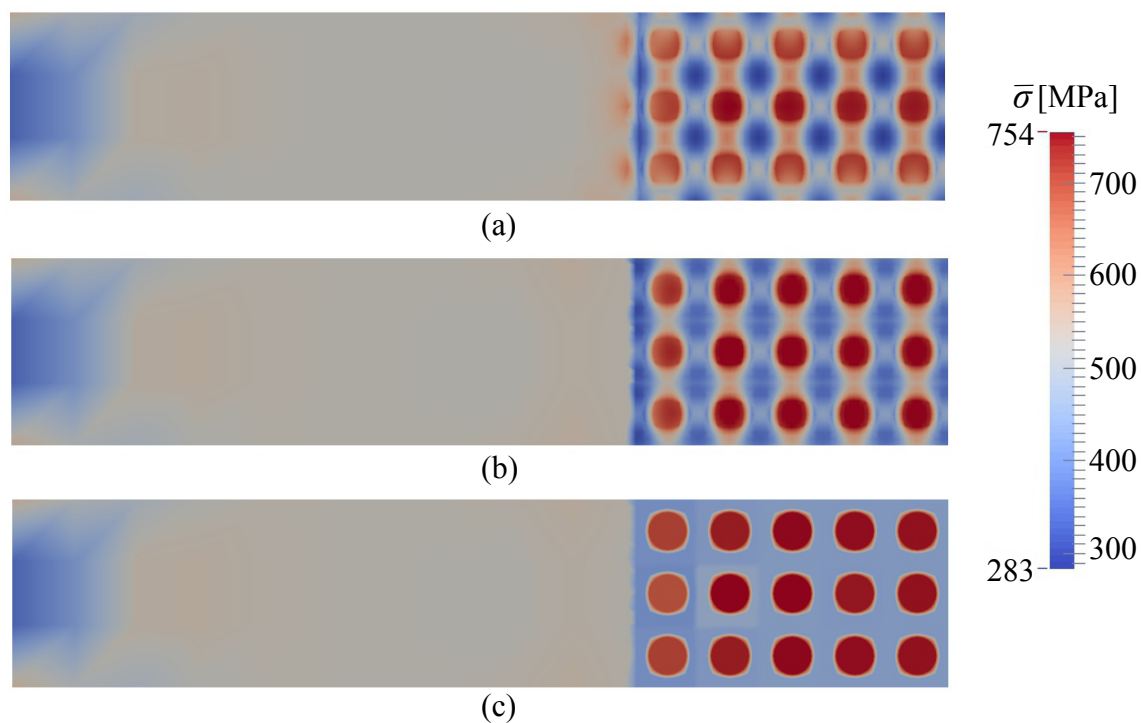
Figure 7: Equivalent stress contours of the specimen with uniform temperature field: (a) finite element model; (b) direct VME model; and (c) ROVME model.
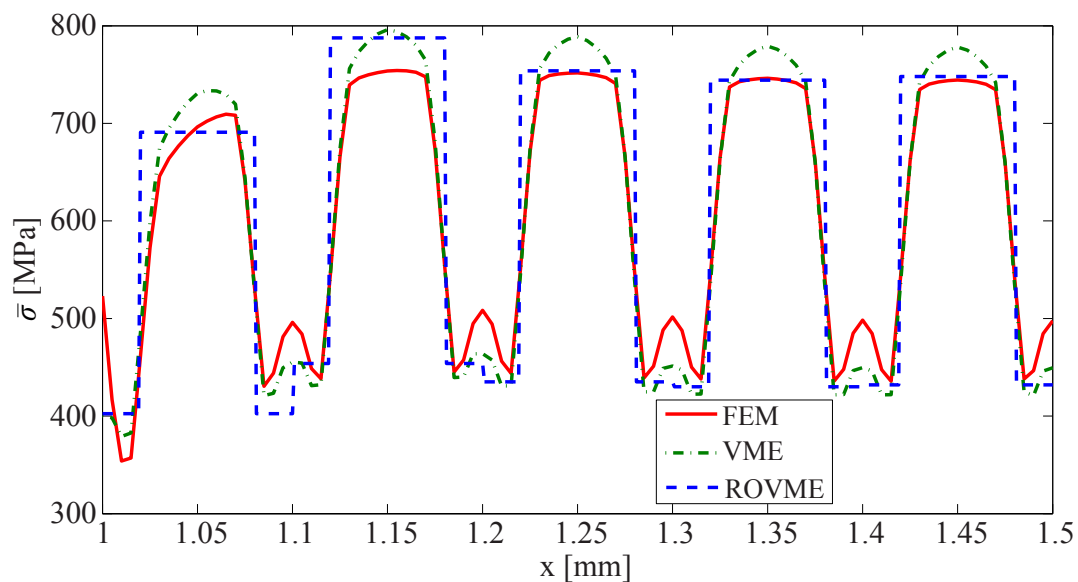

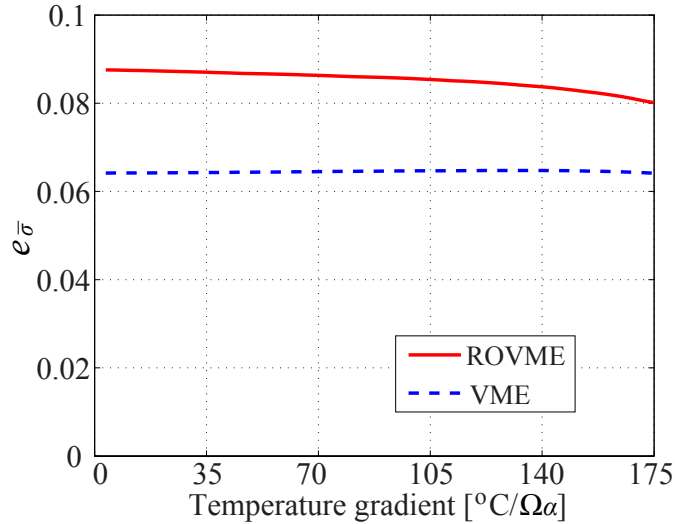Figure 8: Equivalent stresses over a line (x=1.0-1.5 mm, y=0.15 mm) on the specimen with uniform temperature field.

Figure 9: Errors in equivalent stress for the specimen with temperature gradient.

6.2 Specimen subjected to temperature gradient

To further verify the proposed approach, the accuracy is assessed in the context of a specimen subjected to temperature gradient. The mechanical boundary conditions of the specimen are identical to that discussed in Section 6.1. The temperature field $T1$ (in Fig. 5(a) and (b)) along the bottom edge of the specimen linearly increases from 23ºC (at $t = 0$) to 550ºC (at $t = 360$ seconds), while the temperature field $T2$ along the top edge remains constant at 23ºC. The time step size is set to 0.72 second. At the end of the simulation, the temperature variation across an enrichment domain is significant (approximately 175ºC per enrichment domain) which clearly violates the assumption that the temperature field is uniform over each enrichment domain. This example is performed to test the capability of the proposed method at or beyond the limits of the above stated assumptions.

The errors in equivalent stress for the VME and ROVME models are shown in Fig. 9, along with the temperature gradient. The structure remains in the elastic state during the simulation. Both VME and ROVME methods produce higher errors than the previous example (Fig. 6), partially because the uniform temperature field assumption is violated. The stress error of the VME method is stable, while the error of the ROVME method slightly reduces as the temperature gradient increases. The largest error in equivalent stress for the ROVME model is 8.8% and for the direct VME method is 6.5%. The equivalent stress contours of the models at the end of the simulation are shown in Fig. 10, for all of the models. The contours of the direct VME and ROVME models are less smooth than the finite element method, while still closely follow the stress distribution of the reference model. The computational cost for the ROVME simulation is 5.8 minutes while for the finite element simulation is 63.3 minutes.
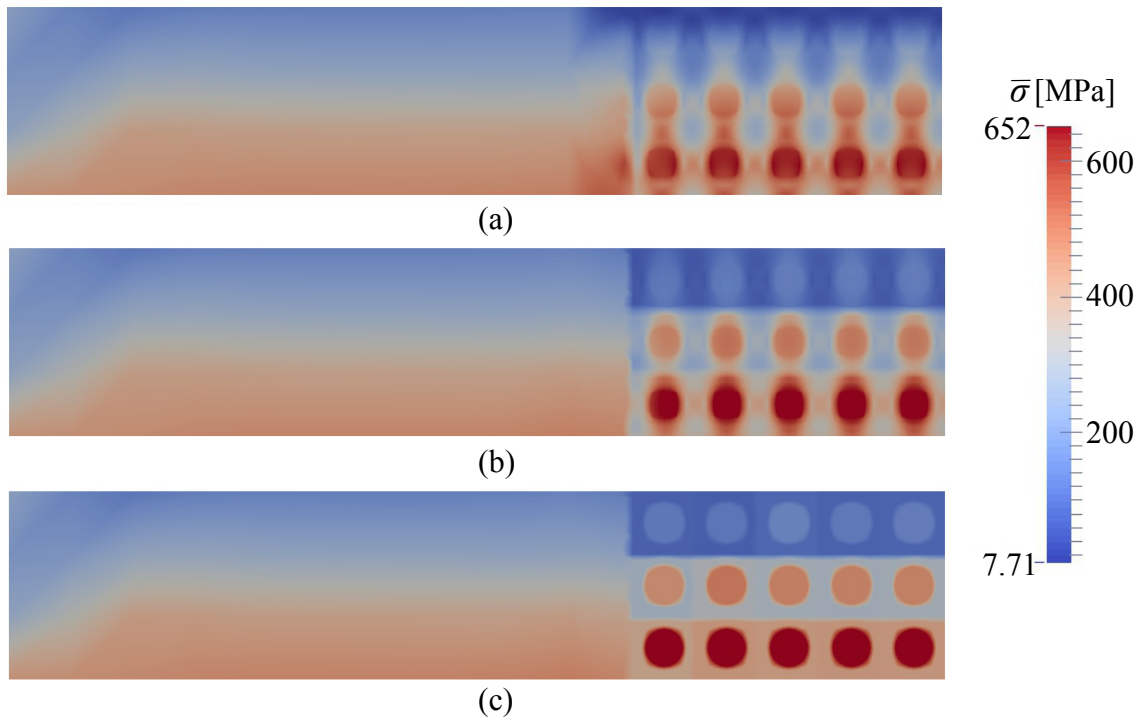
Figure 10: Equivalent stress contours of the specimen with temperature gradient: (a) finite element model; (b) direct VME model; and (c) ROVME model.

The ROVME method is 10.91 times faster than FEM for this example.

6.3 Specimen subjected to combined thermo-mechanical loading

To further study the performance of the proposed methodology, a specimen subjected to combined thermal and mechanical loading is investigated. The time history of the applied boundary conditions $T1$, $T2$ and $\tilde{P}$ are shown in Fig. 11. The bottom and top edges of the specimen are heated at the same rate up to 200ºC and 150ºC, respectively. Then the temperatures are kept constant. Between $t = 270$ - 360 seconds, the specimen is exposed to a monotonically increasing temperature gradient. The specimen is also subjected to a constant boundary pressure of 800 MPa. The time step size of the current example is set to 0.36 second.

The time history of error in equivalent stress is presented in Fig. 12. Until $t = 76$ seconds, the specimen deforms elastically. The inelastic deformation initiates at $t = 76$ seconds, induced by the increasing thermal stress. After $t = 360$, the errors become steady for both VME and ROVME methods, since the loading conditions remain the same and the specimen deforms incrementally elastic at each time step. The maximum error in equivalent stress is 6.6 % for the ROVME method and 4.5% for the VME method.
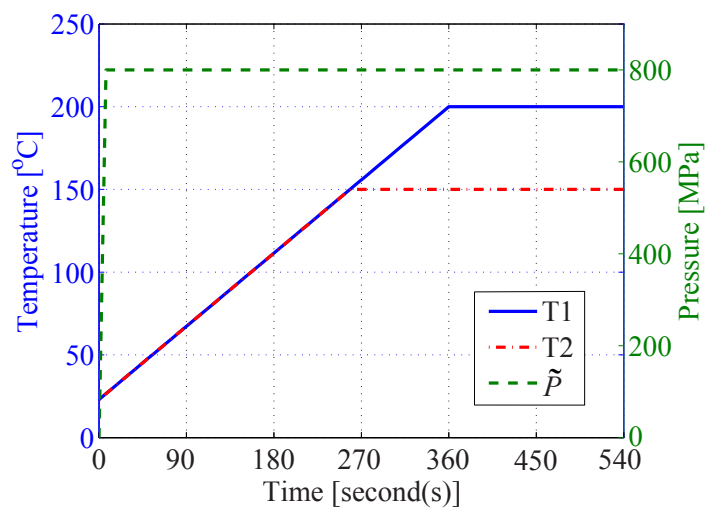
26

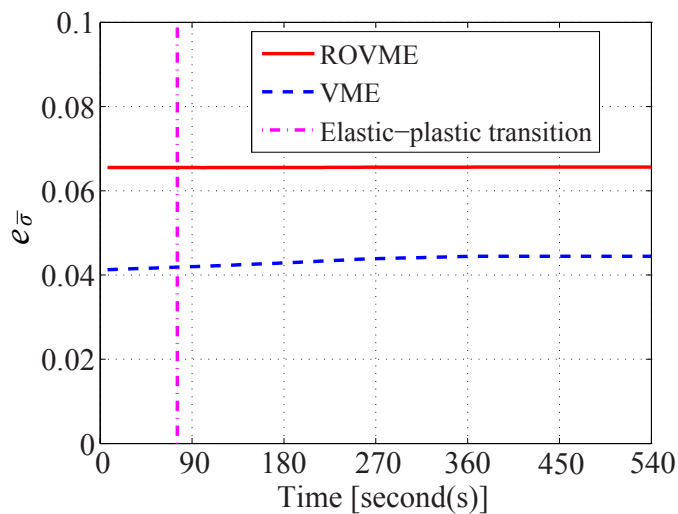Figure 11: Loading conditions of the specimen with pressure.

Figure 12: Errors in equivalent stress for the specimen with pressure.
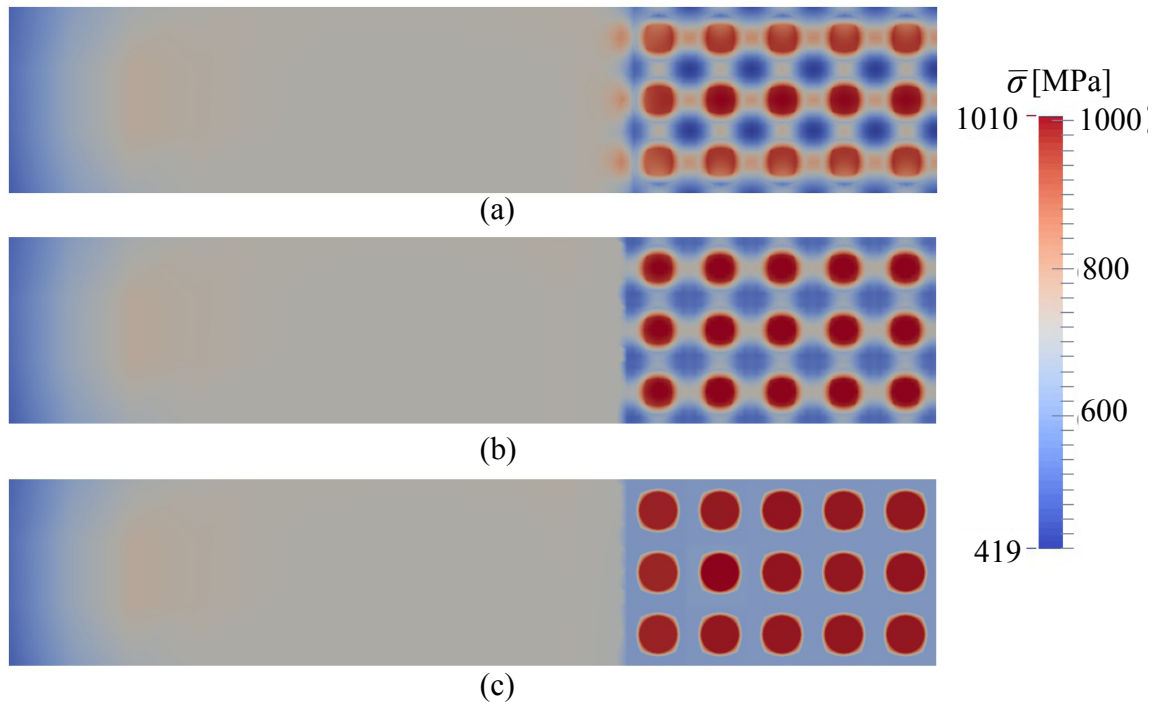
27

Figure 13: Equivalent stress contours of the specimen with pressure: (a) finite element model; (b) direct VME model; and (c) ROVME model.
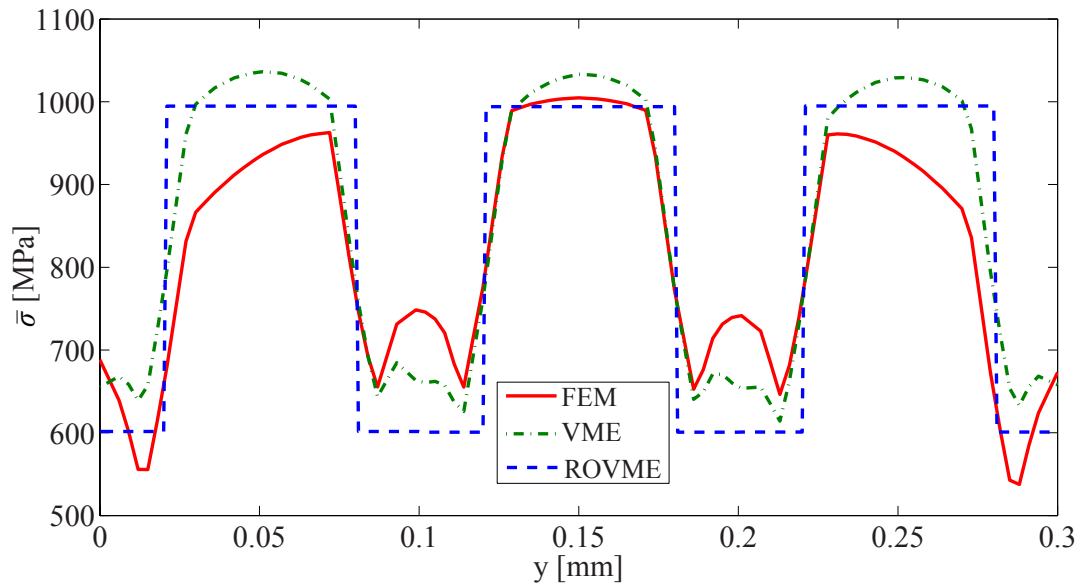

Figure 14: Equivalent stresses over a line (x=1.35 mm, y=0-0.3 mm) on the specimen with pressure.

The stress contours of the reference, VME and ROVME models are shown in Fig. 13. The stress contours of the VME and ROVME approaches are in close agreement with the stress distribution predicted by the reference model. The stress contours are relatively uniform since the pressure load dominates the deformation. The equivalent stress over a line in the enrichment region (x = 1.35 mm, y= 0 - 0.3 mm in Fig. 5(a) and (b)) is plotted for all of the models in Fig. 14.

The stress variation observed between two neighboring inclusions in the FEM approaches are not well captured with the ROVME model, as shown in Fig. 14. This is attributed to the fact that the ROVME model only includes weak interactions between neighboring enrichment domains through the macroscopic equilibrium. The homogeneous Dirichlet boundary conditions employed along the enrichment domain boundaries limit the strong interactions between the neighboring enrichment domains. The accuracy loss could be higher in the presence of stronger inter-enrichment domain interactions, such as in the case of composites with high inclusion volume fractions. Incorporation of more accurate boundary conditions (e.g., mixed boundary conditions proposed in Refs. [41, 56]) could improve the accuracy between two inclusions.

The accuracy of the proposed model is consistent with the previous example in Section 6.1, and demonstrates that both VME and ROVME methods have the capability of accurately capturing the response of structures subjected to combined thermo-mechanical loads. The computational cost for the ROVME simulation is 8.1 minutes while for the finite element simulation is 164.3 minutes. The ROVME model is 20.3 times faster than FEM for this specimen.

The accuracy and efficiency characteristic of the ROVME model is directly related to the model order, NP_α. For instance, Ref. [57] demonstrated that the accuracy could be improved with some loss of efficiency by increasing the model order. We also note that the computational efficiency of the ROVME model is expected to scale with the problem size (i.e., as the number of the enrichment domains within the problem domain increases), as the ratio of the degrees of freedom in the ROVME and direct FEM approaches (as well as the VME approach) increases with the problem size.

7 Functionally Graded Beam

The capabilities of the ROVME approach is further demonstrated by the analysis of a functionally graded composite beam subjected to combined thermo-mechanical loading. The present study builds on the thermo-elastic analysis of functionally graded composites performed by Refs. [47, 48] and extends the analysis to investigate the behavior of the composite within the

Table 2: Materials parameters for zirconia and aluminum of the composite beam

Zirconia	E [GPa]	ν	k [W/mK]	α^T [1×10^{-6}/°C]
	151	0.3	2.09	10.0
Aluminum	E [GPa]	ν	k [W/mK]	α^T [1×10^{-6}/°C]
	70	0.3	204	23
	A [MPa]	B [MPa]	m	n
	517	405	0.41	1.1
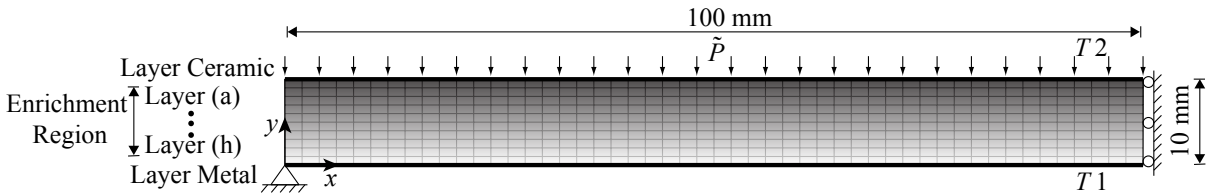
Figure 15: Model sketch and the ROVME macroscale discretization of a functionally graded composite beam under thermo-mechanical loads.
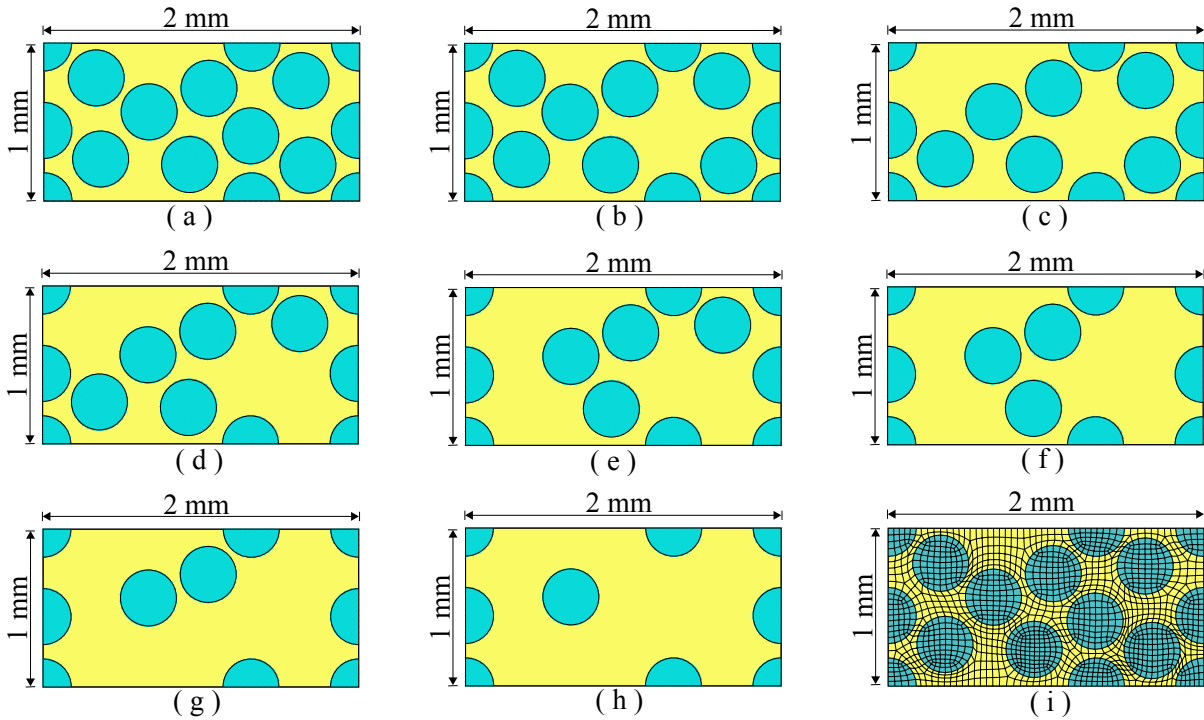

Figure 16: Microscale problems of the ROVME method for layer (a) to layer (h); and (i) microscale discretization for the coefficient tensors computation of layer (a).
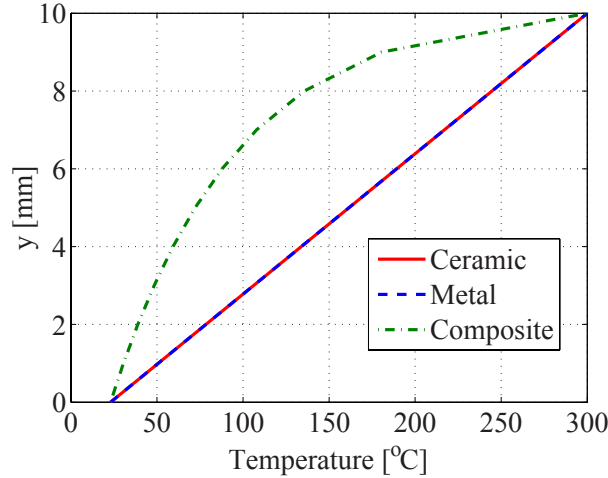
Figure 17: Temperature variations along the thickness of the beam.

plastic regime.

A 2-D, simply supported plane-strain functionally graded beam with length, $a = 200$ mm, and thickness, $t = 10$ mm is considered. The zirconia-aluminum composite is idealized as metal matrix reinforced with randomly positioned ceramic inclusions of circular cross section. The geometry and the boundary conditions are shown in Fig. 15. Due to symmetry, only half of the beam is modeled. The temperatures at the bottom and top edges of the beam, $T1$ and $T2$, are set to 23ºC and 300ºC, respectively. A uniform pressure q_0 is applied on the top of the beam.

The beam is discretized into 500 macroscale quadrilateral finite elements and 561 nodes. The enrichment region is set as the entire domain. The enrichment domains employed are shown in Fig. 16. The top layer of the beam consists of pure zirconia ceramic material and the bottom layer is pure aluminum metal material. From the top to the bottom of the enrichment region (denoted as layer (a) to layer (h) in Fig. 15), the volume fraction of the ceramic in the composite decreases from 55% in layer (a) to 20% in layer (h). The radius of each inclusion is 178.4 μm. The ceramic inclusions remain elastic throughout loading, whereas the metal matrix exhibit inelastic deformations. The Young's moduli of both materials are taken as temperature independent. The material properties for zirconia and aluminum are summarized in Table 2. The room temperature, T_{room}, for both of the materials is set to 23ºC and the melting temperature, T_{melt}, for aluminum is set to 502ºC.

For each of the enrichment domains, a two-part reduced order model is considered. The domains of the parts correspond to the matrix and the inclusion phases. Figure 16(i) shows the microscale mesh employed in pre-processing to compute the coefficient tensors for enrichment domain in layer (a). Similar meshes were used for the other layers. For the purpose of comparison, the reference predictions of two specimens, made of pure aluminum and pure
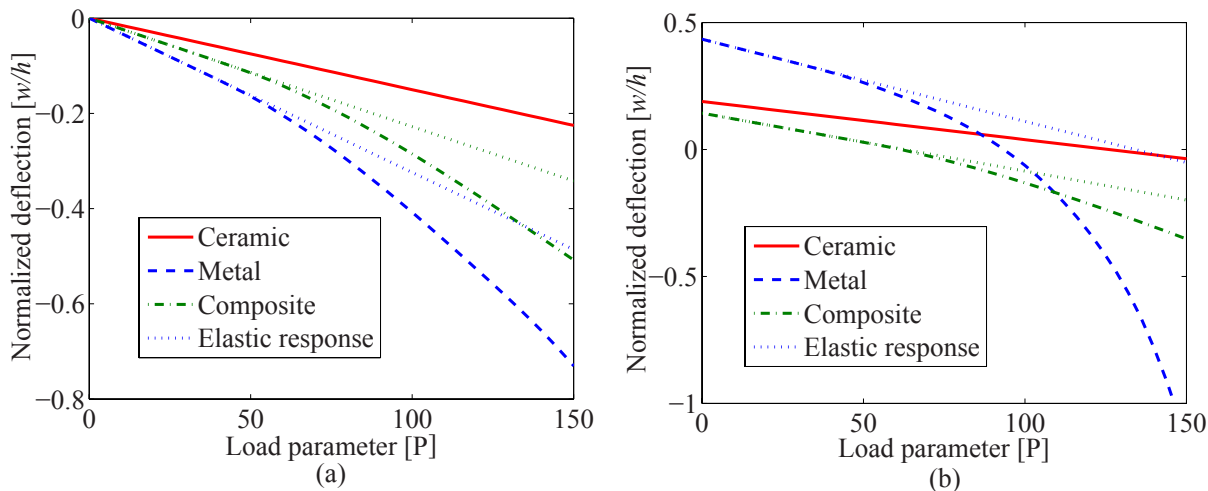
31

Figure 18: Non-dimensional center deflections along with load parameter for beam under: (a) mechanical loading; and (b) thermo-mechanical loading.
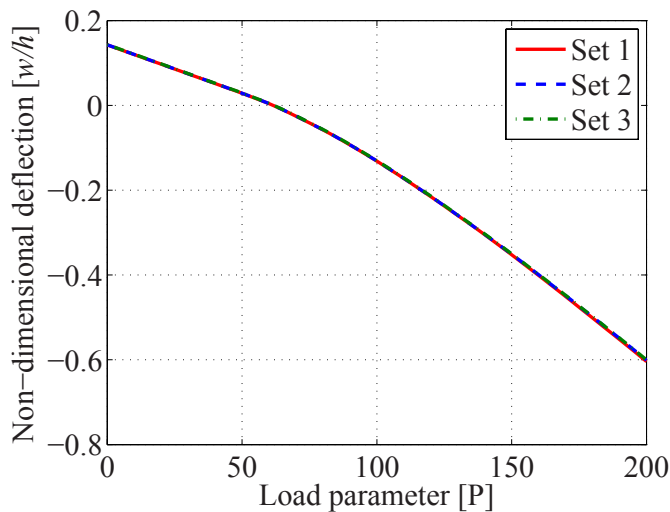

Figure 19: Non-dimensional center deflections along with load parameter for beams using different sets of microstructures.

zirconia, are performed using the finite element method, respectively. Figure 17 shows the steady state distribution of temperature under the prescribed boundary conditions for the monolithic materials and the functionally graded composite. The spatially varying conductivity of the composite beam results in non-linear variation of the temperature field through the thickness. The steady state temperatures within the composite are lower than those in monolithic materials.

Figure 18 presents the normalized deflection, w/h, where w is the deflection of the center of the beam as a function of the normalized load parameter, $P = (q_0 \ a^4)/(E_m \ h^4)$. E_m is the Young's modulus of the metal material and q_0 is taken as 0.01 MPa. Figure 18(a) corresponds to the pure mechanical loading at the room temperature, whereas Fig. 18(b) includes the effect of thermal gradients. In both figures, the dotted lines indicate the responses under the assumption of elastic behavior for both constituents. In the pure mechanical loading, the normalized deflection of the composite beam lies between those of the pure ceramic and pure metal specimens, under both elastic and inelastic material behavior assumptions. The results in Fig. 18(b) include the effect of thermal expansions induced by the temperature gradient over the specimen. In the presence of thermo-mechanical loading, the deflection of the composite beam is lower than both ceramic and metal beams when subjected to moderate mechanical load, under both elastic and inelastic material assumptions. This observation is consistent with those in Refs. [47, 48]. As the load increases, the deflection in the pure metal beam significantly increases due to rapid accumulation of plastic deformation. In contrast, the presence of the ceramic inclusion reduces the amount of plastic flow in the composite specimen, and the rate of deflection remains contained compared with the pure metal specimen.

In order to ensure that the results shown are independent of the microstructural morphology, the thermo-mechanical simulation discussed above is repeated by three separate sets of randomly generated microstructures for each layer of the composite. Figure 19 shows that the overall deflection of the composite is not significantly affected by the microstructural morphology, as long as the volume fraction distribution is maintained.

8 Conclusions

This manuscript provided the reduced order variational multiscale enrichment method (ROVME) for thermo-mechanical problems. The effects of varying thermal state on the mechanical behavior are considered through thermal deformations, temperature-dependent material properties, as well as temperature-dependent flow evolution. In the proposed method, the temperature-dependent coefficient tensors are numerically approximated in order to avoid costly repetitive evaluations at every temperature. The accuracy and computational efficiency characteristics of

33

the proposed ROVME method are verified by comparing with the results of the direct numerical simulations and the VME method. The verification results demonstrate the high accuracy and efficiency of the ROVME method for coupled thermo-mechanical problems. We make the following observations and conclusions: (1) the ROVME approach provides one order of magnitude efficiency compared to direct finite element method with reasonable loss of accuracy, and the efficiency gains are expected to be even higher for larger simulations; (2) the approximation to capture the temperature variation of the coefficient tensors allows the proposed approach to retain the efficiency in the presence of spatio-temporal thermal fluctuations.

9   Acknowledgements

References

[1] *Department of Defense Handbook - Metallic material and elements for aerospace vehicle structures, MIL-HDBK-5J, 31 January 2003.*

[2] J. Aboudi. A continuum theory for fiber-reinforced elastic-viscoplastic composites. *Int. Eng. Sci.*, 20:605–621, 1982.

[3] B. S. Anglin, R. A. Lebensohn, and A. D. Rollett. Validation of a numerical method based on Fast Fourier Fransforms for heterogeneous thermoelastic materials by comparison with analytical solutions. *Comp. Mat. Sci.*, 87:209–217, 2014.

[4] T. Arbogast. Implementation of a locally conservative numerical subgrid upscaling scheme for two-phase Darcy flow. *Comput. GeoSci.*, 6:453–481, 2002.

[5] T. Arbogast. Analysis of a two-scale, locally conservative subgrid upscaling for elliptic problems. *SIAM J. on Numer. Anal.*, 42:576–598, 2004.

[6] D. Bettge, B. Gunther, W. Wedell, P.D. Portella, J. Hemptenmacher, P.W.M. Peters, and B. Skrotzki. Mechanical behavior and fatigue damage of a titanium matrix composite reinforced with continuous SiC fibers. *Mater. Sci. Eng., A*, 452-453:536–544, 2007.

[7] F. Brezzi, L. P. Franca, T. J. R. Hughes, and A. Russo. $b = \int g$. *Comput. Methods Appl. Mech. Engrg.*, 145:329–339, 1997.

[8] N. Carrere, D. Boivin, R. Valle, and A. Vassel. Local texture measurements in a SiC/Ti composite manufactured by the foil-fiber-foil. *Scripta Mater.*, 44:867–872, 2001.

[9] N. Carrere, J.-F. Maire, S. Kruch, and J.-L. Chaboche. Multiscale analysis of SiC/Ti composites. *Mater. Sci. Eng., A*, 365:275–281, 2004.

[10] C. A. Duarte and D. J. Kim. Analysis and applications of a generalized finite element method with global–local enrichment functions. *Comput. Methods Appl. Mech. Engrg.*, 197:487–504, 2008.

[11] G. J. Dvorak. Transformation field analysis of inelastic composite materials. *Proc. R. Soc. Lond. A*, 437:311–327, 1992.

[12] F. Feyel and J. L. Chaboche. FE^2 multiscale approach for modeling the elastoviscoplastic behaviour of long fibre SiC/Ti composite materials. *Comput. Methods Appl. Mech. Engrg.*, 183:309–330, 2000.

[13] L. Figiel and B. Gunther. Modelling the high-temperature longitudinal fatigue behaviour of metal matrix composites (SiC/Ti-6242): Nonlinear time-dependent matrix behaviour. *Int. J. Fatigue*, 30:268–276, 2008.

[14] J. Fish and S. Markolefas. Adaptive global-local refinement strategy based on the interior error estimates of the h-method. *Int. J. Numer. Meth. Engng.*, 37:827–838, 1994.

[15] F. Fritzen and M. Leuschner. Reduced basis hybrid computational homogenization based on a mixed incremental formulation. *Comput. Methods Appl. Mech. Engrg.*, 260:143–154, 2013.

[16] L. Gendre, O. Allix, P. Gosselet, and F. Comte. Non-intrusive and exact global/local techniques for structural problems with local plasticity. *Comput. Mech.*, 44:233–245, 2009.

[17] S. Ghosh and Y. Liu. Voronoi cell finite element model based on micropolar theory of thermoelasticity for heterogeneous materials. *Int. J. Numer. Methods Engrg.*, 38:1361–1398, 1995.

[18] D. Golanski, K. Terada, and N. Kikuchi. Macro and micro scale modeling of thermal residual stresses in metal matrix composite surface layers by the homogenization method. *Comput. Mech.*, 19:188–202, 1997.

[19] T. J. R. Hughes. Multiscale phenomena: Green's functions, the Dirichlet-to-Neumann formulation, subgrid scale models, bubbles and the origins of stabilized methods. *Comput. Methods Appl. Mech. Engrg.*, 127:387–401, 1995.

[20] T. J. R. Hughes, G. R. Feijoo, and J. B. Quincy. The variational multiscale method - a paradigm for computational mechanics. *Comput. Methods Appl. Mech. Engrg.*, 166:3–24, 1998.

[21] A. Hund and E. Ramm. Locality constraints within multiscale model for non-linear material behaviour. *Int. J. Numer. Meth. Engng.*, 70:1613–1632, 2007.

[22] G. R. Johnson and W. H. Cook. Fracture characteristics of three metal subjected to various strain, strain rates, temperatures and pressure. *Eng. Fract. Mech.*, 21:31–48, 1985.

[23] A. S. Khan, A. Yu, and H. Liu. Deformation induced anisotropic responses of Ti-6Al-4V alloy Part II: A strain rate and temperature dependent anisotropic yield criterion. *Int. J. Plasticity*, 38:14–26, 2012.

[24] H. P. Langtangen. *Computational partial differential equations: Numerical methods and diffpack programming.* Springer, 2003.

[25] W. Leclerc, N. Ferguen, C. Plegris, H. Haddad, E. Bellenger, and M. Guessasma. Anumerical investigation of effective thermoelastic properties of interconnected alumina/Al composites using FFT and FE approaches. *Mech. Mater.*, 92:42–57, 2016.

[26] O. Lloberas-Valls, D. J. Rixen, A. Simone, and L. J. Sluys. Domain decomposition techniques for the efficient modeling of brittle heterogeneous materials. *Comput. Methods Appl. Mech. Engrg.*, 200:1577–1590, 2011.

[27] S. Mall and T. Nichols. *Titanium matrix composites: mechanical behavior.* Taylor & Francis, 1997.

[28] K. M. Mao and C. T. Sun. A refined global-local finite element analysis method. *Int. J. Numer. Meth. Engng.*, 32:29–43, 1991.

[29] D. Markovic and A. Ibrahimbegovic. On micro-macro interface conditions for micro scale based FEM for inelastic behavior of heterogeneous materials. *Comput. Methods Appl. Mech. Engrg.*, 193:5503–5523, 2004.

[30] J. C. Michel and P. Suquet. Nonuniform transformation field analysis. *Int. J. Solids Struct.*, 40:6937–6955, 2003.

[31] S. Moorthy, S. Ghosh, and Y.S. Liu. Voronoi cell finite element model for thermoelasto-plastic deformation in random heterogeneous media. *Appl. Mech. Rev.*, 47:207–221, 2001.

[32] M. Mosby and K. Matous. Computational homogenization at extreme scales. *Extreme Mechanics Letters*, 6:68–74, 2016.

[33] C. D. Mote. Global-local finite element. *Int. J. Numer. Meth. Engng.*, 3:565–574, 1971.

[34] H. Moulinec and P. Suquet. A numerical method for computing the overall response of nonlinear composites with complex microstructure. *Comput. Methods Appl. Mech. Engrg.*, 157:69–94, 1998.

[35] A. H. Muliana. Multi-scale framework for the thermo-viscoelastic analyses of polymer composites. *Mech. Res. Commun.*, 35:89–95, 2008.

[36] A. H. Muliana and R. Haj-Ali. A multi-scale framework for layered composites with thermo-rheologically complex behaviors. *Int. J. Solids Struct.*, 45:2937–2963, 2008.

[37] A. K. Noor. Global-local methodologies and their application to nonlinear analysis. *Finite Elements Anal. Des.*, 2:333–346, 1986.

[38] P. O' Hara, C. A. Duarte, T. Eason, and J. Garzon. Efficient analysis of transient heat transfer problems exhibiting sharp thermal gradients. *Comput. Mech.*, 51:743–764, 2013.

[39] J. Oliver, M. Caicedo, A. E. Huespe, J. A. Hernandez, and E. Roubin. Reduced order modeling strategies for computational multiscale facture. *Comput. Methods Appl. Mech. Engrg.*, dx.doi.org/10.1016/j.cma.2016.09.039, 2016.

[40] C. Oskay. Variational multiscale enrichment for modeling coupled mechano-diffusion problems. *Int. J. Numer. Meth. Engng.*, 89:686–705, 2012.

[41] C. Oskay. Variational multiscale enrichment method with mixed boundary conditions for modeling diffusion and deformation problems. *Comput. Methods Appl. Mech. Engrg.*, 264: 178–190, 2013.

[42] C. Oskay and J. Fish. Eigendeformation-based reduced order homogenization for failure analysis of heterogeneous materials. *Comput. Methods Appl. Mech. Engrg.*, 196:1216–1243, 2007.

[43] C. Oskay and M. Haney. Computational modeling of titanium structures subjected to thermo-chemo-mechanical environment. *Int. J. Solids Struct.*, 47:3341–3351, 2010.

[44] L. Ozdemir, W.A.M. Brekelmans, and M.G.D. Geers. FE^2 computational homogenization for the thermo-mechanical analysis of heterogeneous solids. *Comput. Methods Appl. Mech. Engrg.*, 198:602–613, 2008.

[45] H. E. Pettermann, A. F. Plankensteiner, H. J. Bohm, and F. G. Rammerstorfer. A thermo-elasto-plastic constitutive law for inhomogeneous materials based on an incremental mori-tanaka approach. *Comput. Struct.*, 71:197–214, 1999.

[46] A. L. Pilchak, W. J. Porter, and R. John. Room temperature fracture processes of a near-α titanium alloy following elevated temperature exposure. *J. Mater. Sci.*, 47:7235–7253, 2012.

[47] G. N. Praveen and J. N. Reddy. Nonlinear transient thermoelastic analysis of functionally graded ceramic-metal plates. *Int. J. Solids Struct.*, 35:4457–4476, 1997.

[48] J. N. Reddy. Analysis of functionally graded plates. *Int. J. Numer. Meth. Engng*, 47: 663–684, 2000.

[49] J. R. Rice. A metalgorithm for adaptive quadrature. *J. Assoc. Comp. Mach.*, 22:61–82, 1975.

[50] J. R. Rice. Adaptive approximation. *J. Approx. Theory*, 16:329–337, 1976.

[51] S. P. Walker and B. J. Sullivan. Sharp refractory composite leading edges on hypersonic vechicles. *AIAA 20036915, Proceedings of the 12th AIAA International Space Planes and Hypersonic Systems and Technologies, 1519 December 2003, Norfolk, VA.*, 2003.

[52] H. Yan and C. Oskay. A three-field (displacement-pressure-concentration) formulation for coupled transport-deformation problems. *Finite Elements Anal. Des.*, 90:20–30, 2014.

[53] Q. Yu and J. Fish. Multiscale asymptotic homogenization for multiphysics problems with multiple spatial and temporal scales: a coupled thermo-viscoelastic example problem. *Int. J. Solids Struct.*, 39:6429–6452, 2002.

[54] J. Yvonnet and Q.-C. He. The reduced model multiscale method (R3M) for the non-linear homogenization of hyperelastic media at finite strains. *J. Comput. Phys.*, 223:341–368, 2007.

[55] H. W. Zhang, S. Zhang, J. Y. Bi, and B. A. Schrefler. Thermo-mechanical analysis of periodic multiphase materials by a multiscale asymptotic homogenization approach. *Int. J. Numer. Meth. Engng*, 69:87–113, 2007.

[56] S. Zhang and C. Oskay. Variational multiscale enrichment method with mixed boundary conditions for elasto-viscoplastic problems. *Comput. Mech.*, 55:771–787, 2015.

[57] S. Zhang and C. Oskay. Reduced order variational multiscale enrichment method for elasto-viscoplastic problems. *Comput. Methods Appl. Mech. Engrg.*, 300:199–224, 2016.

[58] X. Zhang and C. Oskay. Eigenstrain based reduced order homogenization for polycrystalline materials. *Comput. Methods Appl. Mech. Engrg.*, 297:408–436, 2015.

A Appendix

This appendix provides the implementation of the VME method within an arbitrary enrichment domain, Ω_α. The starting point is the rate form of the constitutive equation which is obtained by taking the time derivative of the constitutive equation:

$$
\begin{aligned}
\dot{\boldsymbol{\sigma}} = \mathbf{L}(T) : &\left[\dot{\boldsymbol{\varepsilon}}^M(\mathbf{u}^M) + \sum_{\alpha=1}^{n_{\text{en}}} \mathcal{H}(\Omega_\alpha)\, \dot{\boldsymbol{\varepsilon}}_\alpha^m(\mathbf{u}_\alpha^m) - \dot{\boldsymbol{\varepsilon}}^{vp}(\boldsymbol{\sigma}, \mathbf{u}^M, \mathbf{u}^m) - \boldsymbol{\alpha}^T\, \dot{T} \right] \\
&+ \left(\frac{\partial \mathbf{L}(T)}{\partial T}\, \dot{T} \right) : \left[\boldsymbol{\varepsilon}^M(\mathbf{u}^M) + \sum_{\alpha=1}^{n_{\text{en}}} \mathcal{H}(\Omega_\alpha)\, \boldsymbol{\varepsilon}_\alpha^m(\mathbf{u}_\alpha^m) - \boldsymbol{\varepsilon}^{vp}(\boldsymbol{\sigma}, \mathbf{u}^M, \mathbf{u}^m) - \boldsymbol{\alpha}^T\, (T - T_0) \right] \\
= \mathbf{L}(T) : &\left[\dot{\boldsymbol{\varepsilon}}^M(\mathbf{u}^M) + \sum_{\alpha=1}^{n_{\text{en}}} \mathcal{H}(\Omega_\alpha)\, \dot{\boldsymbol{\varepsilon}}_\alpha^m(\mathbf{u}_\alpha^m) - \dot{\boldsymbol{\varepsilon}}^{vp}(\boldsymbol{\sigma}, \mathbf{u}^M, \mathbf{u}^m) - \boldsymbol{\alpha}^T\, \dot{T} \right] \\
&+ \dot{T}\, \frac{\partial \mathbf{L}(T)}{\partial T} : \mathbf{L}(T)^{-1} : \boldsymbol{\sigma}
\end{aligned}
\tag{68}
$$

Perform the discretization of the viscoplastic slip evolution using a one-parameter family (θ-rule):

$$
\dot{\boldsymbol{\varepsilon}}^{vp}(\mathbf{x}, T, t) = (1 - \theta)\dot{\boldsymbol{\varepsilon}}^{vp}(\mathbf{x},\,_n t) + \theta\dot{\boldsymbol{\varepsilon}}^{vp}(\mathbf{x},\,_{n+1} t); \quad t \in [_n t,\,_{n+1} t]
\tag{69}
$$

Substituting Eq. (69) into Eq. (68), the time discretization of the constitutive equation in rate form yields:

$$
\begin{aligned}
\mathbf{R}(\boldsymbol{\sigma}, \mathbf{u}^M, \mathbf{u}^m) \equiv &\,_{n+1}\boldsymbol{\sigma} - \,_n\boldsymbol{\sigma} - \,_{n+1}\mathbf{L} : \Delta\boldsymbol{\varepsilon}^M - \sum_{\alpha=1}^{n_{\text{en}}} \mathcal{H}(\Omega_\alpha)_{n+1}\mathbf{L} : \Delta\boldsymbol{\varepsilon}_\alpha^m \\
&+ (1 - \theta)\Delta t \,_{n+1}\mathbf{L} : \,_n\dot{\boldsymbol{\varepsilon}}^{vp} + \theta\Delta t \,_{n+1}\mathbf{L} : \,_{n+1}\dot{\boldsymbol{\varepsilon}}^{vp} + \,_{n+1}\mathbf{L} : \boldsymbol{\alpha}^T\, (_{n+1}T - T_0) \\
&- \,_{n+1}\left(\frac{\partial \mathbf{L}}{\partial T} \right) : \,_{n+1}\mathbf{L}^{-1} : \,_{n+1}\boldsymbol{\sigma}\, (_{n+1}T - \,_n T) = 0
\end{aligned}
\tag{70}
$$

where, $\Delta\boldsymbol{\varepsilon}^M = \,_{n+1}(\nabla\mathbf{u}^M) - \,_n(\nabla\mathbf{u}^M)$ and $\Delta\boldsymbol{\varepsilon}_\alpha^m = \,_{n+1}(\nabla\mathbf{u}_\alpha^m) - \,_n(\nabla\mathbf{u}_\alpha^m)$. The temperature field $(_{n+1}T)$ and tensor of elastic moduli $(_{n+1}\mathbf{L} = \mathbf{L}(_{n+1}T))$ are known at the current time step $(_{n+1}t)$. The time derivative of the elastic tensor of moduli $(\partial\mathbf{L}/\partial T)$ is evaluated numerically. In the rest of the current section, the subscript $n + 1$ of the fields at the current configuration is omitted for clarity of presentation. Approximate Eq. (70) using a first order Taylor series expansion for a Newton iteration yields the residual of the stress-strain equation:

$$
\begin{aligned}
\mathbf{R}^{k+1} \approx \mathbf{R}^k + &(\mathbf{I} + \theta\, \Delta t\, \mathbf{L} : \mathbf{C}^k - \mathbf{D}) : \delta\boldsymbol{\sigma} + \theta\, \Delta t\, \mathbf{L} : \mathbf{G}^k : \delta\boldsymbol{\varepsilon}^{vp} - \mathbf{L} : \nabla(\delta\mathbf{u}^M) \\
&- \sum_{\alpha=1}^{n_{\text{en}}} \mathcal{H}(\Omega_\alpha)\mathbf{L} : \nabla(\delta\mathbf{u}_\alpha^m) = 0
\end{aligned}
\tag{71}
$$

40

where, the operators $\mathbf{C}^k$, $\mathbf{G}^k$ and $\mathbf{D}$ are defined as:

$$\mathbf{C}^k = \left(\frac{\partial \dot{\boldsymbol{\varepsilon}}^{vp}}{\partial \boldsymbol{\sigma}}\right)^k; \quad \mathbf{G}^k = \left(\frac{\partial \dot{\boldsymbol{\varepsilon}}^{vp}}{\partial \boldsymbol{\varepsilon}^{vp}}\right)^k; \quad \mathbf{D} = \left(\frac{\partial \mathbf{L}}{\partial T}\right) : \mathbf{L}^{-1}\left(T - {}_n T\right) \tag{72}$$

The detailed formulation of $\mathbf{C}^k$ and $\mathbf{G}^k$ can be found in Ref. [56]. Taylor series approximation does not include the derivative respect to the temperature field, since it is taken as a known variable for the mechanical problem. The residual of the kinematic equation (Eq. (69)) is defined as:

$$\mathbf{P} \equiv {}_{n+1}\boldsymbol{\varepsilon}^{vp} - {}_n\boldsymbol{\varepsilon}^{vp} - \Delta t\,(1-\theta)\,{}_n\dot{\boldsymbol{\varepsilon}}^{vp} - \Delta t\,\theta\,{}_{n+1}\dot{\boldsymbol{\varepsilon}}^{vp} = 0 \tag{73}$$

Performing linearization of Eq. (73), the viscoplastic strain increment is expressed in terms of the stress increment as:

$$\delta\boldsymbol{\varepsilon}^{vp} = (\mathbf{I} - \theta\,\Delta t\,\mathbf{G}^k)^{-1} : (\theta\,\Delta t\,\mathbf{C}^k) : \delta\boldsymbol{\sigma} - (\mathbf{I} - \theta\,\Delta t\,\mathbf{G}^k)^{-1} : \mathbf{P}^k \tag{74}$$

Substituting Eq. (74) into Eq. (71), the viscoplastic strain is condensed out to represent the stress increment at the current Newton iteration as:

$$\delta\boldsymbol{\sigma}(\delta\mathbf{u}^M, \delta\mathbf{u}_\alpha^m) = \hat{\mathbf{L}}^k : \nabla(\delta\mathbf{u}^M) + \sum_{\alpha=1}^{n_{\text{en}}} \mathcal{H}(\Omega_\alpha)\,\hat{\mathbf{L}}^k : \nabla(\delta\mathbf{u}_\alpha^m) - \mathbf{Q}^k : (\mathbf{R}^k - \mathbf{Z}^k) \tag{75}$$

where,

$$\hat{\mathbf{L}}^k = (\mathbf{L}^{-1} + \theta\,\Delta t\,\mathbf{C}^k - \mathbf{L}^{-1} : \mathbf{D} + \mathbf{L}^{-1} : \mathbf{H}^k)^{-1} \tag{76}$$

$$\mathbf{Q}^k = (\mathbf{I} + \theta\,\Delta t\,\mathbf{L} : \mathbf{C}^k - \mathbf{D} + \mathbf{H}^k)^{-1} \tag{77}$$

$$\mathbf{H}^k = (\theta\Delta t)^2\,\mathbf{L} : \mathbf{G}^k : (\mathbf{I} - \theta\,\Delta t\,\mathbf{G}^k)^{-1} : \mathbf{C}^k \tag{78}$$

$$\mathbf{Z}^k = \theta\,\Delta t\,\mathbf{L} : \mathbf{G}^k : (\mathbf{I} - \theta\,\Delta t\,\mathbf{G}^k)^{-1} : \mathbf{P}^k \tag{79}$$

Substituting Eq. (75) into the linearized weak form equilibrium equations for the macroscale and microscale problems, a coupled two-scale system of equations is obtained and solved through finite element discretization. The structural responses are determined incrementally using Newton-Raphson iterative scheme. At each iteration, the two scales are evaluated sequentially by taking the known solution of the other scale. Detailed formulation and implementation can be found in Ref. [56]. They are skipped in the current manuscript for brevity.